An Approach for Active Gust Load Alleviation by Means of Dynamic Flaps

Journal:	*Journal of Aircraft*
Manuscript ID	2022-06-C037086
Manuscript Type:	Full Paper
Date Submitted by the Author:	13-Jun-2022
Complete List of Authors:	Ullah, Junaid; University of Stuttgart, Institute of Aerodynamics and Gas Dynamics Radespiel, Rolf; Technische Universität Braunschweig, Institute of Fluid Mechanics Lutz, Thorsten; University of Stuttgart, Institute of Aerodynamics and Gas Dynamics Klug, Lorenz; TU Braunschweig, Institute of Fluid Mechanics Wild, Jochen; DLR German Aerospace Center, Institute of Aerodynamics and Flow Technology Heinrich, R.; German Aerospace Center DLR Institute of Composite Structures and Adaptive Systems, Multidisciplinary Modeling
Subject Index Category:	00100 Aerodynamics < 00000 AIRCRAFT TECHNOLOGY, CONVENTIONAL, STOL/VTOL, 20500 Computational Fluid Dynamics < 20000 FLUID DYNAMICS, 01210 Flow Control < 00000 AIRCRAFT TECHNOLOGY, CONVENTIONAL, STOL/VTOL

An Approach for Active Gust Load Alleviation by Means of Dynamic Flaps

Junaid Ullah * and Thorsten Lutz†
University of Stuttgart, Institue of Aerodynamics and Gas Dynamics, Stuttgart, 70569 Stuttgart

Lorenz Klug ‡ and Rolf Radespiel§
Technische Universität Braunschweig, Institute of Fluid Mechanics, Braunschweig, 38108, Germany

Jochen Wild¶ and Ralf Heinrich ‖
German Aerospace Center (DLR), Braunschweig, 38108 Germany

Active Gust Load Alleviation techniques exhibit a high potential in significantly reducing the transient gust loads on aircraft. In this work the aerodynamic potential of dynamic Trailing Edge Flaps and Leading Edge Flaps is numerically studied with the purpose to significantly reduce the structural gust loads. The utilized spanwise segmented flaps represent slight modifications of existing devices for high-lift and maneuvering. The investigations based on unsteady RANS computations are conducted by employing a generic wing-fuselage aircraft configuration at transonic flow conditions. Idealized discrete "$1-\cos$" type vertical gusts that are relevant for the certification process are used as representative atmospheric disturbances. The focus of this paper is to introduce a practicable prediction method for required trailing and leading edge flap deflections for a significant mitigation of gust induced wing loads. The 3D flap deflections are determined by parametric 2D simulations at representative wing sections. Different extensions of the estimation approach are investigated to assess the influence of the wing planform, the finite wing span, the aerodynamic phase lags and the flap scheduling. It is shown that the trailing and leading edge flaps are promising in terms of alleviation of gust induced wing bending and wing torsional moments, respectively. However, at high leading edge flap deflections that are necessary for a full compensation of the wing torsional moment large scale flow separation is identified. The introduced active gust load alleviation approach indicates a good transferability between 2D airfoil and 3D wing aerodynamics for dynamic flap deflections.

*Research Assistant, Institue of Aerodynamics and Gas Dynamics, Pfaffenwaldring 21, 70569 Stuttgart
†Research Scientist, Institue of Aerodynamics and Gas Dynamics, Pfaffenwaldring 21, 70569 Stuttgart
‡Research Assistant, Institute of Fluid Mechanics, Hermann-Blenk Str.37,38108 Braunschweig, l.klug@tu-braunschweig.de
§Professor and Head of Institue of Fluid Mechanics, Hermann-Blenk Str.37, 38108 Braunschweig
¶Head of Transport Aircraft Department, DLR Institute of Aerodynamics and Flow Technology, Lilienthalpl.7, 38108 Braunschweig
‖Team Leader Multidisciplinary Modeling, DLR Institute of Aerodynamics and Flow Technology, Lilienthalpl.7, 38108 Braunschweig

Nomenclature

Abbreviations

AGLA	=	Active Gust Load Alleviation
CFD	=	Computational Fluid Dynamics
CSD	=	Computational Structural Dynamics
DLR	=	German Aerospace Center
DVA	=	Disturbance Velocity Approach
FAA	=	Federal Aviation Administration
FAR25	=	Federal Aviation Regulations 25
FM	=	Flight Mechanics
IATA	=	International Air Transport Association
LEF	=	Leading Edge Flap
LU-SGS	=	Lower-Upper Symmetric Gauss-Seidel
RANS	=	Reynolds-Averaged Navier-Stokes
RBF	=	Radial Basis Function
SAO	=	Spalart-Allamaras Original
TEF	=	Trailing Edge Flap
TM	=	Turbulence Model
WBM	=	Wing Bending Moment
WTM	=	Wing Torsional Moment

Symbols

α	=	angle of attack, (°)
b	=	wing span, (m)
c	=	chord length, (m)
C_D	=	drag coefficient 3D simulations, (-)
C_L	=	lift coefficient 3D simulations, (-)
c_L	=	lift coefficient 2D simulations or local sectional lift coefficient at span station γ, (-)
c_M	=	pitching moment coefficient 2D simulations or local sectional moment coefficient at span station γ, (-)
$C_{M,y}$	=	pitching moment coefficient 3D simulations, (-)
c_{ref}	=	mean aerodynamic chord, (m)
C_{WTM}	=	coefficient of wing torsional moment, (-)
C_{WBM}	=	coefficient of wing bending moment, (-)

CoP = center of pressure, (-)

φ = wing leading edge sweep, (°)

$\varphi_{50\%c}$ = wing sweep at 50% chord, (°)

F_g = flight profile alleviation vector, (-)

γ = normalized spanwise coordinate $y/(0.5b)$, (-)

H = flight altitude, (m)

k = reduced frequency, (-)

M = Mach number for 3D configuration, (-)

η = flap deflection, (°)

λ_{Gust} = gust wavelength, (m)

ω = angular frequency, (rad/s)

S = reference wing area, (m^2)

t = time, (s)

t_{conv} = convective time of flow, (s)

U = vertical gust velocity, (m/s)

U_∞ = inflow velocity, (m/s)

U_{ds} = design gust velocity, (m/s)

U_{ref} = reference gust velocity, (m/s)

x, y, z = Cartesian coordinates, (m)

y^+ = non-dimensional wall distance, (-)

I. Introduction

Total CO_2 emissions from all commercial operations totaled 918 million metric tons in 2018 [1]. That is 2.4% of global green house gas emission and a 32% increase over the past five years. In 2009, the International Air Transport Association (IATA) set three goals for reducing CO_2 emissions from aviation: (1) an average improvement in fuel efficiency of 1.5% per year from 2009 to 2020, (2) carbon-neutral growth after 2020, and (3) a 50% reduction in net aviation CO_2 emissions by 2050, compared to the levels of 2005 [1]. All three emission goals imply a strong interest of aircraft manufacturers in reducing the structural weight of commercial aircraft. Gust induced loads during cruise flight represent dimensioning loads for structural design of aircraft [2]. Current airworthiness requirements (Federal Aviation Regulations 25 (FAR25)) of the Federal Aviation Administration (FAA) [3] prescribe a proof of structural integrity for response of the aircraft to encounters with discrete and continuous gusts. Concepts for reducing gust loads represent promising measures to meet the emission goals set by the IATA and reduce passenger discomfort. While

passive methods like additional stiffness of the wing structure are established, drastic load reductions are only possible by developing effective approaches for Active Gust Load Alleviation (AGLA), which are designed to instantaneously compensate the transient loads induced by the inhomogeneous wind fields. Especially a multifunctional usage of already existing control surfaces which are used for high-lift and maneuvering purposes is promising with regard to minimizing additional structural modifications, system complexity and actuation requirements. An incorporation of the active control technology for maneuver and gust load alleviation from the onset of the aircraft pre-design allows to reduce the wing bending moments, structural mass and extend the fatigue life [4]. The ultimate goal is a full compensation of critical transient gust loads by trimming the loads toward a load factor of one throughout the unsteady gust event ("1g wing").

Numerous AGLA systems have been successfully integrated, for example on the following airplanes: Lockheed C-5A, Lockheed L-1011-500, Boeing B-1, Northrop Grumman B-2, Airbus A320, Airbus A330/A340, Airbus A380, Boeing 787, Airbus A350. An overview of application of active controls to mitigate gust response is presented in [5]. AGLA systems on operational aircraft, for which information is available in the public domain, mostly utilize control surfaces on the outboard wing, such as ailerons and spoilers as well as rudders and elevators on the horizontal empennage. AGLA systems investigated during flight tests and experiments which aim at a reduction of structural wing loads comprise ailerons and segmented flaps. Other AGLA concepts are designed for damping of the aircraft's rigid body motion and elastic modes. Furthermore, Regan et al. have given an interesting overview and reference list of investigations of AGLA applications in wind tunnel and flight tests in [5].

Most of the aforementioned flap based techniques to reduce structural wing loads make use of an approach based on lift redistribution along the wing span by employing steady flap deflections. A reduction of the wing root bending moment is initiated by a shift of the local lift forces toward the wing root. Numerical and experimental studies used this concept to demonstrate its potential for both gust load alleviation [2, 6, 7] and maneuver load alleviation [8, 9]. Besides application to operational aircraft, dynamic trailing edge flaps for maneuver load alleviation and gust load alleviation are investigated at low speed conditions both experimentally and numerically e.g. in [10–13]. Dynamic leading edge flaps were investigated at low speed conditions for maintaining attached flow during scenarios which represent flight maneuvers or gust interactions [14]. However, investigations of AGLA concepts at transonic speeds are rare and include mainly trailing edge flaps [2, 15, 16] or dynamic ailerons for load redistribution [6].

Other more recent types of AGLA concepts include flaps on the fuselage [7], bumps at the nose region of the wing [17], fluidic actuators [18], micro-spoiler [18], morphing wings [19], and hinged or folding wing tip devices [20–23]. The elevators of the horizontal tail plane can also be used for AGLA purposes. A turning of the whole aircraft toward the wing can reduce the induced velocities and thus the structural loads.

No control strategies are applied in this work, as we suggest full knowledge of the aircraft reaction to well defined discrete gust scenarios. Control mechanisms and their benefits on gust load control were studied intensively in recent

years, e.g. in [19, 24–28]. These studies demonstrate the high potential of improved control strategies with respect to AGLA.

Gust loads also cause aeroelastic deformations of the wing, which can lead to self-excited aeroelastic instabilities so called flutter. Flutter can lead to airframe failure caused by divergent oscillations. A thorough overview of research and developments in the active flutter operation are can be found in [29]. Besides an overview of active flutter suppression mechanisms, the latter work also contains the developments and the state of the arts of the supporting disciplines, i.e., maneuver load control, gust load control, aeroservoelastics, active buffet control, aircraft morphing etc.. No aeroelasticity is considered in the present work. Therefore, no further investigation of aeroelastic related issues are covered here. The reasons for this neglect and potential consequences are discussed later in Sec. II.B.

Most integrated AGLA systems use inertial accelerometers or inclination measurements to estimate the gust induced loads and initiate a reactive response. At transonic flight a higher load alleviation performance can be achieved by a better forecast of the near future loads. This can be realized by measuring and processing the wind field ahead of the aircraft by e.g. Doppler LIDAR sensors [30, 31]. The basic idea for the gust load alleviation using a Doppler LIDAR sensors is that the measured atmospheric disturbances can be processed to estimate the structural loads and initiate the AGLA systems before the gust reaches the wing of the aircraft and induces additional loads. Aircraft exposed to high true air speeds necessitate a measurement of the gust far upstream of the aircraft to provide a sufficient lead time for real time actuation of the AGLA systems. Besides an overcoming of the AGLA system inertia, a consideration of the angular velocities of the flaps, the transmission speed of the feedforward and feedback control system, and a potential phase lag between the actuated systems and their reaction needs to be considered. Modern Doppler LIDAR systems permit to measure the wind 60-300 m ahead of the aircraft nose [30]. This gives a lead time which is stated as sufficient based on slew rates and maximum deflections feasible by ailerons.

In the present paper, the AGLA approach is based on purely dynamic flap deflections with the objective to push the local spanwise loads during the gust encounter toward the condition prevailing at standard cruise conditions. This means that the benefit of a spanwise load redistribution is deliberately ignored. Recent studies by the author of the paper at hand [32] have shown that a combination of both initial steady flap deflections and superimposed dynamic flap deflections are superior when compared to the individual approaches. While the first introduces a beneficial load redistribution towards the inboard wing the second further reduces the loads during the direct gust interaction. This combination allows improvements especially in terms of reduced flap deflection rates and maximum flap deflection amplitudes for a full suppression of gust induced wing loads. However, the main objective of the present paper is to present a practical method which allows to predict the required maximum flap deflection angles for a reduction of the Wing Bending Moment (WBM) and the Wing Torsional Moment (WTM) as introduced by a predetermined gust scenario. While the concept of spanwise load redistribution by spanwise segmented Trailing Edge Flaps (TEF) and Leading Edge Flaps (LEF) allows a very high number of variations in case no optimization algorithm is applied, the

concept of AGLA by dynamic flap deflections studied here specifies a clear target spanwise lift and pitching moment distribution at each time step throughout the gust interaction. Thus, the latter AGLA method is predestined to evaluate a prediction strategy for the required flap deflection amplitudes based on a representative 2D airfoil database.

The studies presented by Ullah et al. in [33], where solely dynamic flaps are utilized for gust alleviation purposes at transonic flow conditions, laid the foundation for this work. In the same work 2D airfoil simulations demonstrate the high potential of TEF regarding the control of the lift force. It is well known that for supercritical (transonic) airfoils the concave shape on the rear end of the pressure side significantly contributes to lift ("rear loading"), which makes trailing edge flaps (TEF) very promising regarding compensation of gust induced lift. Ullah et al. [33] also demonstrate the efficiency of 2D LEF deflections for the compensation of the gust induced pitching moment. It is also shown that the efficiencies of the TEF and the LEF as derived from 2D airfoil simulations can be transferred to the 3D wing where the spanwise segmented TEF and the LEF reveal a high impact on the WBM and WTM, respectively. Furthermore, it was also demonstrated in [33] that the supersonic flow region on an aircraft wing shows high dependencies on dynamic TEF and LEF deflections that lead to fundamental differences in the flap efficiencies when compared to application at subsonic conditions. These preliminary 2D and 3D studies helped to establish a degree of confidence in the actuator concepts discussed in the present work. The work at hand continues to build on these results by increasing the vertical gust velocities toward the specifications prescribed in the certification process [3] and applying a more sophisticated and matured concept for the 2D-3D data transformation. The presented simulations in [33] were conducted at a gust velocities which are approx. 70% of the gust velocities required in the FAR25 and the 2D database consists of simulations at only one representative wing section.

The present paper is structured as follows: The second section II introduces the research configuration and the flow conditions followed by a short overview of the numerical setup and a thorough description of the procedure to determine the dynamic flap deflections to compensate the load dominant gust loads. The results section III is divided into four parts. First, a gust-prestudy is presented to derive the critical gust loads for the wing structure III.A. Afterwards a validation of the investigated AGLA concept is conducted III.B. The subsequent sections include the application of the AGLA on the aircraft configuration III.C and an overall assessment of all force and moment coefficients III.D. The last results section contains the impact of different extensions and simplifications of the AGLA concept III.E. The paper is closed by a summary of the conclusions IV.

II. Setup

The most relevant information regarding the research model, the inflow conditions, and the numerical approach is summarized in the present paper. For more detailed information the reader is referred to [33].

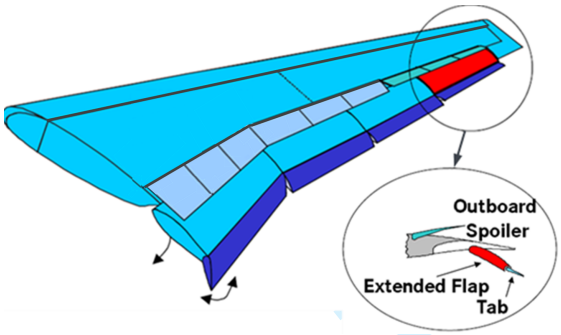

(a) Integration of movable tabs into high lift devices [35]

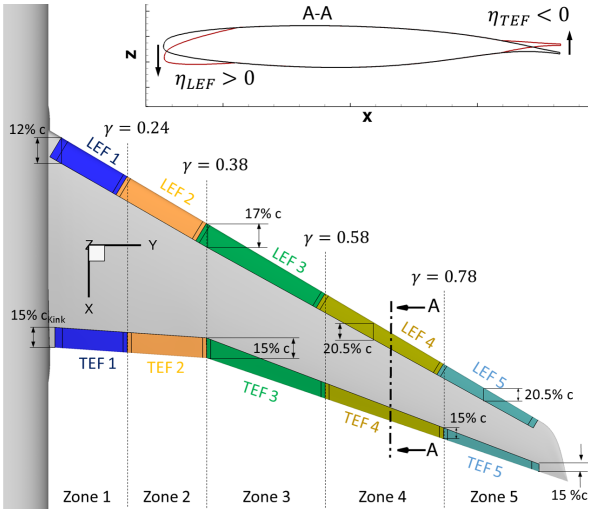

(b) Illustration of segmented TEF and LEF on the wing of the LEISA configuration and representative airfoil section with definition of signs for LEF and TEF deflections η.

Fig. 1 Illustration of segmented TEF and LEF for AGLA.

A. Geometric Configuration

The research configuration used for the assessment of the AGLA concepts is a wing-fuselage representation of the DLR LEISA configuration [34], which is a short to medium range, single aisle twin engine aircraft. The setup of the control surfaces, as depicted in Fig. 1(b), is derived from the wing with multifunctional control surfaces developed during the German Pro-HMS project [35], see Fig. 1(a). The spanwise segmented tabs at the end of the Fowler flaps were designed for active control of maneuver and gust loads. This approach is transferred to the LEISA configuration by applying a local flap chord length of 15%c to the TEF in the midspan region where c is the local chord length of the local wing section. Inboard from the kink the chord length of the TEF is consistent with the TEF's chord length at the kink, which is 15% c_{kink}. The most outboard TEF (TEF 5) has also a chord length of approx. 15%c which is 60% of the aileron's chord length. The chord length for the LEF of 20% c in the outboard region, 17% c at the kink, and 12% c in the proximity of the fuselage is equivalent to the one of the wing slat. In the paper at hand the LEF deflections were realized similar to droop nose deflections. Possible losses in the high lift performance by utilizing droop noses along the full wing span are neglected here for this preliminary concept study. The rotation axes or hinge lines of the TEF and the LEF are assumed to be located at the center of the respective upper and lower edge points of each flap. As transient gust loads lead to spatial variations of the local aerodynamic forces and moments acting on the wing structure, the LEF and the TEF are segmented along the wing span for locally optimized load alleviation. The TEF and the LEF are divided into five spanwise segments based on a minimum variation from the spanwise extensions of the LEISA high-lift devices and evaluations of spanwise gust load variations. The 2D simulations for the prediction of the required 3D flap amplitudes were performed by using representative airfoil sections along the span, as exemplarily illustrated in

the top right corner of Fig. 1. Based on the conventions for deflection angles η of high lift devices, a negative TEF deflection describes an upward directed motion and a positive LEF deflection describes a downward directed motion. The reference wing area S_{ref} of 172 m^2 and the reference chord length c_{ref} of 5.15 m are used for normalization of the forces and moments of the 3D configuration. The reference chord is located at approximately 50% wing span. The relative lengths of the flaps are plotted in Fig. 1(b).

In this work we neglect limitations of the flap deflection speeds based on the maximum angular velocities which for the TEF can be derived from slew rates of ailerons and for the LEF from slew rates of droop noses. Furthermore, we presume that the characteristics of the wind field sufficiently ahead of the aircraft are available. Thus, dynamic flap deflections can even be initiated before the gust impinges the aircraft, if necessary. The purpose is to identify the full aerodynamic potential of the combined flap concept without restricting boundary conditions from actuator and measurement systems.

The main evaluation criteria in this work are the gust induced structural wing loads. Two physical quantities are considered to represent these loads, namely the Wing Bending Moment (WBM) and the Wing Torsional Moment (WTM). The WBM is evaluated about the global moment reference point, which is located at 45%c at the wing root. It is equivalent to the roll moment of the wing about the global moment reference point of the wing-fuselage LEISA configuration. The WTM is calculated in a postprocessing step by a spanwise integration of the local pitching moments derived from the airfoil sections parallel to the x, z-plane, see Fig. 2. The reference line for the WTM is the 45% local chord, as this is the assumed location of the neutral axis of the wing box on the 3D configuration. Per definition the computation of the WTM utilizes the moments on the airfoil sections perpendicular to the wing's neutral axis. Thus, the WTM in the way computed for the investigations in this study is not equivalent to the structural WTM as defined in the literature as it includes a component of the bending moment. The reasons for selecting a somewhat different definition for the WTM is based on a simplified transferability between the spanwise local pitching moment and the global WTM. This is crucial for the conversion between 2D simulations conducted at wing sections parallel to the xz-axis and the 3D simulations. In terms of non-dimensional coefficients, this gives the following definition for the WTM:

$$C_{WTM} = \int_{y_{root}}^{y_{tip}} \frac{c_M(y)\ c(y)^2}{S_{ref}\, c_{ref}} dy = \frac{1}{S_{ref}\, c_{ref}} \sum_{i=1}^{200} c_{M,i}\, c_i^2\, \Delta y, \tag{1}$$

where S_{ref} and c_{ref} denote the reference wing area and the reference chord length. The integral is approximated via a sum using local pitching moment coefficient c_M evaluations at 200 equally distributed spanwise airfoil sections. The reference point for the local pitching moment c_M is also located at 45% local chord.

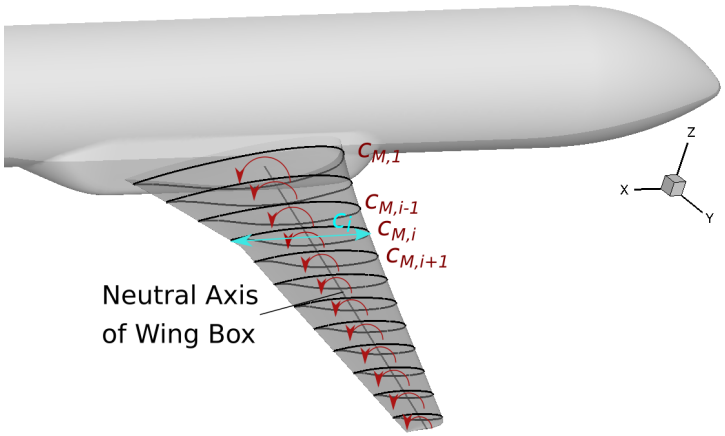

Fig. 2 Integration of C_{WTM} from local spanwise c_M.

B. Flow Conditions and Computational Approach

The cruise flight conditions for the LEISA configuration are given as Mach number $M = 0.8$, altitude $H = 35000$ ft and lift coefficient $C_L = 0.5$. The unstructured finite volume compressible flow solver DLR TAU [36] is used for the unsteady RANS simulations. A cell-vertex dual cell grid approach is utilized to transform the computational grid before the computation. A central scheme of second order accuracy is chosen for spatial discretization. Temporal resolution of second order is achieved by selecting an implicit Backward Euler method with Lower-Upper Symmetric Gauss-Seidel (LU-SGS) scheme as linear solver. The Spalart-Allmaras Original (SAO) one-equation Turbulence Model (TM) is used to close the system of RANS equations for the viscous computations. Laminar to turbulent transition is neglected throughout this work and the flow is simulated fully turbulent. No laminar to turbulent transition is considered throughout this work. The time step size for the computations with dual time stepping scheme are chosen based on the deflection period of the flaps and the gust wave length λ_{Gust}. It was demonstrated by internal studies of the time step convergence that 150 time steps per actuation period suffice to reproduce the unsteady response of the aircraft, even if this means a reduction by a factor of approx. seven compared to the typically considered 100 physical time steps per convective time ($t_{conv} = U_\infty/c$). A number of 400 inner iterations per physical time step were used to guarantee a sufficient convergence within the inner iteration cycle. TAU uses local time stepping and a multigrid scheme for convergence acceleration. A 3-level W-cycle is chosen for the latter in this work.

The flap deflections are realized by a component based mesh deformation via Radial Basis Function (RBF) interpolation with a volume spline. This requires a displacement field of the actuator surfaces relative to the baseline geometry for each computed time step. RBF's do not require connectivity information among interpolated points (so-called scattered data interpolation), which gives them a high efficiency for smooth functions [37]. A base point reduction algorithm is implemented in TAU allowing a significantly lower number of entries in the deformation matrix. In this work the displacement vectors for the flap deformation are computed by a simple rotation of the effective

surfaces which result from connecting the trailing edge points with the hinge line points of the flaps. More sophisticated approaches, like the one introduced by McDaniel et al. in [38] represent a more realistic rotation of the flaps, especially in the hinge region. However, due to the moderate deflection angles for the flaps considered in this work, the benefit in modeling a more accurate flap rotation is negligible. The spanwise gaps between deflected flaps and the non-deflected wing sections are neglected to avoid usage of complex Chimera or sliding interface meshing strategies. The gaps are closed by a smooth cos -blending which is effective in preventing negative grid cell volumes.

The Disturbance Velocity Approach (DVA) is used for gust modeling [39]. Compared to a resolved gust approach, the DVA allows a usage of standard CFD grids and thus a significant reduction in computational resources. In the DVA the gust velocities are considered by an alteration of the flux balances through superposition of the disturbance velocity field. Several studies show that the DVA is proven to accurately capture airfoil-gust interaction for large gust wave lengths ($>> c$). Heinrich et al. [39] demonstrate that the DVA's lift respones is accurate for consecutive NACA0012 airfoils at sub- and transonic speeds as well as for a generic wing-fuselage configuration at transonic speeds for gust wave lengths larger than twice the chord length. Consecutive investigations by Müller et al. [40, 41] assess the influence of gust wavelength and angle of attack variations on the DVA's accuracy regarding lift, drag and pitching moment of a single airfoil for sub- and transonic gust interaction. It is shown that the DVA provides reliable results for these parameters. Deviations in the DVA results occur for small wavelengths $\lambda_{Gust} \leq c$ or high angles of attack. While the subsonic investigations [41] include a variation of the airfoil shape, the transonic investigations [40] utilize the DLR-F15 airfoil which is the reference airfoil for the LEISA configuration. The transonic inflow conditions are also comparable to the ones used within this work providing a strong evidence for the reliability of the current DVA results. The gust scenarios within this work fulfill the requirements on wavelength and angle of attack for the DVA to be accurate. For the presented simulations the gust was introduced into the flow field at least five characteristic length scales (c_{ref}) upstream from the aircraft.

In accordance with the aircraft regulations in the Federal Aviation Regulations Part 25 (FAR25) of the FAA [3] "1 − cos" gust velocity shapes with a vertical gust velocity of

$$U = \frac{U_{ds}}{2}\left[1 - \cos\left(\frac{2\pi x}{\lambda_{Gust}}\right)\right] \quad \text{for } 0 \leq x \leq \lambda_{Gust} \quad \& \quad U = 0\,\text{m/s} \quad \text{for } x > \lambda_{Gust} \tag{2}$$

are utilized. The design gust velocities U_{ds} increase with the wave length according to

$$U_{ds} = U_{ref}\, F_g \left(\frac{\lambda_{Gust}}{214}\right)^{1/6}. \tag{3}$$

The reference gust velocity U_{ref} and the flight profile alleviation vector F_g are a function of flight altitude as described in [3]. F_g is conservatively assumed to be equal to one, which means that the aircraft operates 100% of the time at the

cruise altitude. According to the FAR25 definition U_{ref} is defined in equivalent airspeed and needs to be converted in true airspeed. Figure 3 shows typical vertical "1 − cos" type gust shapes covering the λ_{Gust} range defined in the FAR25 from 18 m-214 m. The dashed line illustrates the envelope of the design gust velocities for the depicted gust velocity profiles. Both vertical or lateral gust velocities with positive and negative amplitudes have to be considered in the certification process [3]. However, as vertical gusts with a positive amplitude represent the critical design condition for the structural loads on the wing, they are selected as relevant gust conditions in this work. Vertical gusts with positive amplitude add up to the loads already acting on the wing structure during undisturbed cruise conditions.

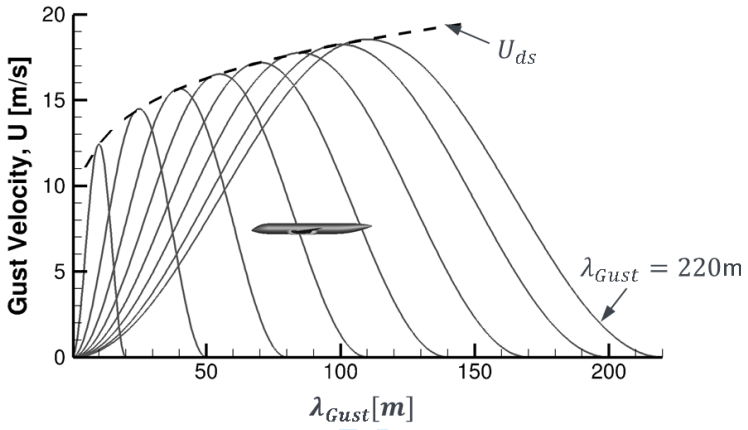

Fig. 3 Typical "1 − cos" design gust velocity profiles according to FAR25 [3].

The computational grids consist of approximately 20 million grid points. A symmetric half model of the wing-fuselage LEISA configuration is used for the computations. The hybrid unstructured grid of the LEISA configuration is generated with the commercial mesh generator CENTAUR (v14.5) by CentaurSoft. The grid consists of triangular surface elements, a prismatic grid to resolve the boundary layer, and a tetrahedral mesh in the remaining domain. Approximately 50 prismatic layers cover the boundary layer. A non-dimensional wall distance of $y^+ < 1$ is fulfilled for the first prismatic wall layer on each geometric component. The grid volume on the suction side of the wing is additionally refined with isotropic tetrahedral elements to allow for an adequate resolution of the sharp gradients caused by the shock waves. More detailed information on the composition of the computational grid can be found in [33].

The aerodynamic efficiencies of the flaps are studied under consideration of the viscous, transonic, and the three dimensional unsteady effects. The most significant simplification in the presented simulations is the neglect of the aeroelasticity and flight mechanics, which affect the gust response of the aircraft. The analysis of gust load alleviation techniques usually necessitates a multidisciplinary approach of a CFD code with a Computational Structural Dynamics (CSD) and Flight Mechanics (FM) code that are coupled in the time domain. Nevertheless, coupled CFD-CSD-FM simulations are still too computationally expensive despite thee incessant increase in computational power, especially when considering their utilization during the preliminary design process. Therefore, the common practice in aircraft

industry for simulating gust and maneuvering loads is the usage of software with low fidelity potential flow theory codes for the aerodynamic computation, like panel codes or Doublet Lattice Method (DLM) codes, instead of state-of-the-art CFD codes. It is well known that transonic and viscous aerodynamic effects at cruise flight conditions of airliners are not captured by potential flow codes, let alone the highly unsteady effects going along with a gust encounter. It is shown by Reimer et al. in [42] that gust loads predicted with CFD are significantly lower than those of the classical DLM-based methods not only at transonic, but also in the subsonic flow regime. Published CFD-CSD-FM works related to gust load prediction and gust load alleviation, such as [6, 39, 43], focus on individual load scenarios and load alleviation concepts to demonstrate the capability of the coupled approach. The results discussed in this paper are based on pure CFD, which will allow a more extended parametric study of the AGLA concepts. Furthermore, a computational domain with high resolution will allow a deeper insight into flow physics resulting from gust-aircraft-flap interaction. A neglect of the aircraft motion and the aeroelasticity resulting from gust encounter leads to a too conservative approach for the flap design. Simulations at similar flow conditions as used for this work demonstrate a drop in the vertical load factor of 25%-35% when comparing CFD-standalone simulations with a coupled CFD-FM-CSD approach, see [39, 42]. These studies also reveal that these differences are mostly of a quantitative nature when neglecting the transient response and decay effects after the gust encounter. As introduced in the next section, the investigated AGLA approach aims at a full mitigation of the WBM and WTM by aligning the spanwise lift and pitching moments toward the baseline cruise condition throughout the gust event. In case of an ideal alignment of the spanwise lift the vertical motion of the aircraft is prevented with the further assumption that the change in the global pitching moment introduced by the gust and the flap deflections can be trimmed by the elevator of the HTP. Furthermore, a mitigation of the spanwise lift and pitching moment implies a small aeroelastic deformation of the wing. These considerations suggest a valid representation of both qualitative and quantitative time-response to an idealized "1 − cos" gust-event by CFD mono-disciplinary simulations for the application in the present paper.

C. Prediction of 3D Flap Deflections based on Strip Theory

In this section the estimation of the 3D flap deflection angles is described by employing unsteady 2D simulations which are adapted via theory of infinite swept wings. Furthermore, the applied flap schedulings including the phase shifts are introduced. Additional approaches which consider more complex flap time schedulings and 3D effects are discussed later in the results section (Sec. III.E). The basis for the estimation are computationally efficient 2D simulations which are conducted by employing the airfoil sections at planes normal to the y-axis from each spanwise center of the five wing zones, see Fig. 1 (b). An exception was made for the airfoil located at the spanwise center of zone 1 where the airfoil of the zone 2 was used with adjusted chord length and flap dimensions. The airfoils in the root region are designed to counter the local 3D effects by recreating isobars which are parallel to the leading edge. Thus, 2D simulations of the original root airfoils can not capture the local flow characteristics. By generally using the

different airfoils at all five wing zones a compliance with the local airfoil geometries, the local Reynolds numbers and the chordwise flap extensions are guaranteed. A method where representative 2D sections of the wing are extracted for the prediction of the 3D flow characteristics is referred to as strip theory in most literature [44]. First general reflections on the 2D-3D transformation problem are presented before introducing the estimation procedure employed for the prediction of the 3D flap deflections.

1. Alignment of the Baseline Cruise Condition between 2D and 3D Results

No generally applicable theory exists for the transformation of 2D airfoil aerodynamics to 3D wing planforms in case of tapered swept and twisted wings with finite span at transonic viscous flow conditions. Opinions about the applicability of the swept-wing theory at transonic and viscous flow conditions differ. A review of swept-wing theory at transonic speeds by Bendiksen [45] suggests inherent differences between nonlinear transonic aerodynamics and linear subsonic aerodynamics. Therefore, the discard of the spanwise component in the calculations of lift and moment can lead to incorrect results as soon as the Mach number exceeds the critical Mach number [45]. However, the work of Pätzold [46] indicates that the impact of the temperature dependency at transonic conditions, which deteriorates the principle of independence between the tangential flow and normal flow components, is rather moderate for wing sweeps up to 30°. Furthermore, the assumption that the influence of the Reynolds stresses on the velocity gradients in spanwise direction, which also reduces the validity of the principle of independence, is less effective for pressure distributions from RANS simulations. Therefore, the swept-wing theory can be applied for specific boundary conditions even at viscous and transonic flows.

Wing tapering strongly reduces the accuracy of the above mentioned 2.5D transformation, which simply uses an unified sweep angle. An extension of the 2.5D swept-wing theory is introduced by Streit et al. [47] for the wing tapering. The method is based on sectional conical wing solutions which are denoted as 2.75D solutions. Lock [48] proposed that 2D and 3D pressure distributions are similar for a swept-tapered wing, if the distribution of the Mach number components normal to the isobars are identical. It is assumed that the isobars are fully swept and follow the lines of constant x/c. An optimization design method based on the equations of Lock [48] and the conical approach of Streit et al. [47] was developed by Zhao et al. [49]. It considers the variation of the local sweep angle in streamwise direction and the local curvature of a tapered swept wing. This method shows an improved agreement between 2D and 3D pressure distributions when compared to the traditional 2.5D transformation. It is also demonstrated that the derived 2.75D formulations are applicable to transonic conditions by treating the flow upstream and downstream of the shock wave as isentropic and using the normal shock wave relations for determining the pressure loss across the shock wave. Because the pressure distribution is largely affected by the wing root effect, the different trailing edge sweep at $y < y(kink)$, the wing tip effect and the 3D flow at the kink, only the part of the wing somewhat outboard from the kink and inboard from the tip (from approx. 45% to 85% of the half-span) can be regarded as a quasi-conical flow region.

Due to this reason the increased effort in applying the 2.75D theory is not reasonable. Furthermore, for the assessment of the flap efficiencies on the 3D wing a similarity in both local spanwise lift and pitching moment distributions at undisturbed cruise conditions is essential, which is not achievable through the 2.75D theory. Studies form Streit et al. [47] suggest a good agreement between 2.75D and 2.5D results for transonic applications in case the shock wave location line instead of the quarter chord is selected as effective sweep angle for the 2.5D theory. The shock wave location is approximately at 50% chord for the investigated flow conditions and the reference wing. For the reasons mentioned above, an adapted method building on the 2.5D theory with the effective sweep being the sweep at the shock position is introduced next to allow a tolerable agreement between 2D and 3D data for the application in this work.

Based on the theory of infinite swept wings the airfoil sections are transformed into the wing's normal section by vertically stretching the airfoil with the factor $1/\cos(\varphi_{50\%c})$, which leads to an increased relative thickness of the airfoil. The effective sweep angle $\varphi_{50\%c}$ for the transformation between the 2D airfoil data and the 3D wing data, corresponds to the angle of the 50%c line at the outboard wing. Besides the stretching of the airfoil section, the representative sweep angle $\varphi_{50\%c}$ was also applied to transform the inflow Mach number M, the flap angles η, the gust wave length λ, the angle of attack α and consequently also the local lift and pitching moment coefficient c_L and c_M as follows

$$\begin{aligned}
M_{2.5D} &= M_{2D}/\cos\varphi_{50\%c} \\
c_{2.5D} &= c_{2D}/\cos\varphi_{50\%c} \\
\lambda_{2.5D} &= \lambda_{2D}/\cos\varphi_{50\%c} \\
\alpha_{2.5D} &= \alpha_{2D} \times \cos\varphi_{50\%c} \\
c_{L,2.5D} &= c_{L,2D} \times \cos^2\varphi_{50\%c} \\
c_{M,2.5D} &= c_{M,2D} \times \cos^2\varphi_{50\%c} \\
\tan(\eta_{2.5D}) &= \tan(\eta_{2D}) \times \cos\varphi_{50\%c}.
\end{aligned} \tag{4}$$

The index 2.5D denotes variables which are transformed into the line of flight wing sections and thus represent 3D data. Additionally, angle of attack iterations were utilized for the 2D simulations to match the local lift values of the 3D simulations

$$\alpha_{2D} = \alpha(c_{L,2D}). \tag{5}$$

This led to an exact agreement between 2D and 3D c_L and to an improved agreement between 2D and 3D c_M when compared to results without c_L alignment. Only the spanwise c_L and c_M distributions at baseline cruise conditions without deployed flaps were selected for the first assessments of the 2D-3D transformation. Therefore, a validation of the 2D database for deflected flaps is presented in Sec. III.B.

2. Step by Step Description of the Procedure for AGLA

In the following section a thorough description of the simulation steps used for the prediction of the required 3D TEF and LEF deflections is given. The approach is presented by working through the illustrations in Fig. 4. For reasons of clarity the illustration only shows the evaluation at zone 3, see Fig. 1(b). The real application necessitates an evaluation of all of the five wing zones. We aim at strong control authority over the WBM and WTM moment by aligning the instantaneous spanwise c_L and c_M toward the cruise condition throughout the gust event. Simultaneously, the impact on the other forces and moments acting on the aircraft configuration should be kept within the limits given by the gust loads. This excludes unintended reactions of the aircraft to the dynamic TEF and LEF deflections.

The foundation of the AGLA approach is a 2D database which is generated through simulations of dynamic TEF and LEF deflections at undisturbed inflow conditions for all of the five extracted airfoils. More details about the 2D database are covered later in the results section (Sec. III.C). In the following the three steps of the 3D simulations depicted in Fig. 4 are described including the evaluated parameters.

1) The first step of the actual AGLA evaluation process is the simulation of the aircraft-gust interaction without deployed TEF and LEF. The simulations are conducted for a critical representative gust scenario. For the estimation of the maximum TEF 3 deflection angle on the 3D wing the reference evaluation point is the maximum gust induced WBM in zone 3, see top left plot in Fig. 4. The averaged difference between the spanwise c_L distributions at the time of the maximum WBM and at the cruise condition in zone 3 allows to calculate the required deflections of the TEF 3 on the 3D wing. This is done by employing the TEF 3 efficiencies in $\Delta C_{L,2D}$ from the 2D database and a subsequent 2D-3D data transformation as described in the previous section. A linear interpolation method is used to provide an assumption for TEF angles in between the computed 2D data points.
2) A short introduction of the flap time functions is presented first, which is applicable to both dynamic TEF and LEF deflections. The flap deflection time coincides with the convective time of the gust over the respective wing section by following a "1 − cos" function. The time functions of the flap scheduling takes into account that the gust interacts with the wing segments in a delayed manner due to the wing sweep. The consideration of the real time response of the aircraft as resulting from the simulations of gust interaction is deliberately excluded for the determination of the flap period due to the large unrepresentative decay times. An analysis of the wing loads to flap time functions which are directly derived from the time histories of the gust induced loads is presented as extended method in Sec. III.E. Furthermore, the phase shifts $\Delta t_{\text{phase shift,i}}$ at each wing zone i resulting from the gust response, see top left image in Fig. 4, are also considered in the final flap scheduling. The delayed reaction (phase lag) or premature reaction (phase lead) to TEF and LEF deflections in the peak loads is also extracted from the 2D simulations and added to the phase shift from the gust response. The results of the phase shifts introduced by 2D TEF and 2D LEF deflections are

presented later in Sec. III.C. The final time function for dynamic flap deflection angles η_{Flap} is defined as follows:

$$\eta_{\mathrm{Flap,i}}(t) = \frac{\eta_{\mathrm{Flap,i,max}}}{2}\left[1 - \cos\left(\frac{2\pi(t - \Delta t_{\mathrm{i}} \pm \Delta t_{\mathrm{phase\ shift,i}})}{\lambda_{\mathrm{Gust}}/U_{\infty}}\right)\right] \quad \text{for} \quad 0 \le t - \Delta t_i \pm \Delta t_{\mathrm{phase\ shift,i}} \le \lambda_{\mathrm{Gust}}/U_{\infty}$$
$$\& \quad \eta_{\mathrm{Flap,i}}(t) = 0 \quad \text{for} \quad t - \Delta t_i \pm \Delta t_{\mathrm{phase\ shift,i}} > \lambda_{\mathrm{Gust}}/U_{\infty} \tag{6}$$
$$\& \quad \eta_{\mathrm{Flap,i}}(t) = 0 \quad \text{for} \quad t - \Delta t_i \pm \Delta t_{\mathrm{phase\ shift,i}} < 0.$$

The maximum dynamic flap deflection angles $\eta_{\mathrm{Flap,max}}$ along the span are estimated based on the 2D database and the 2D-3D transformation method described in this section. The time needed by the gust to travel the distance from

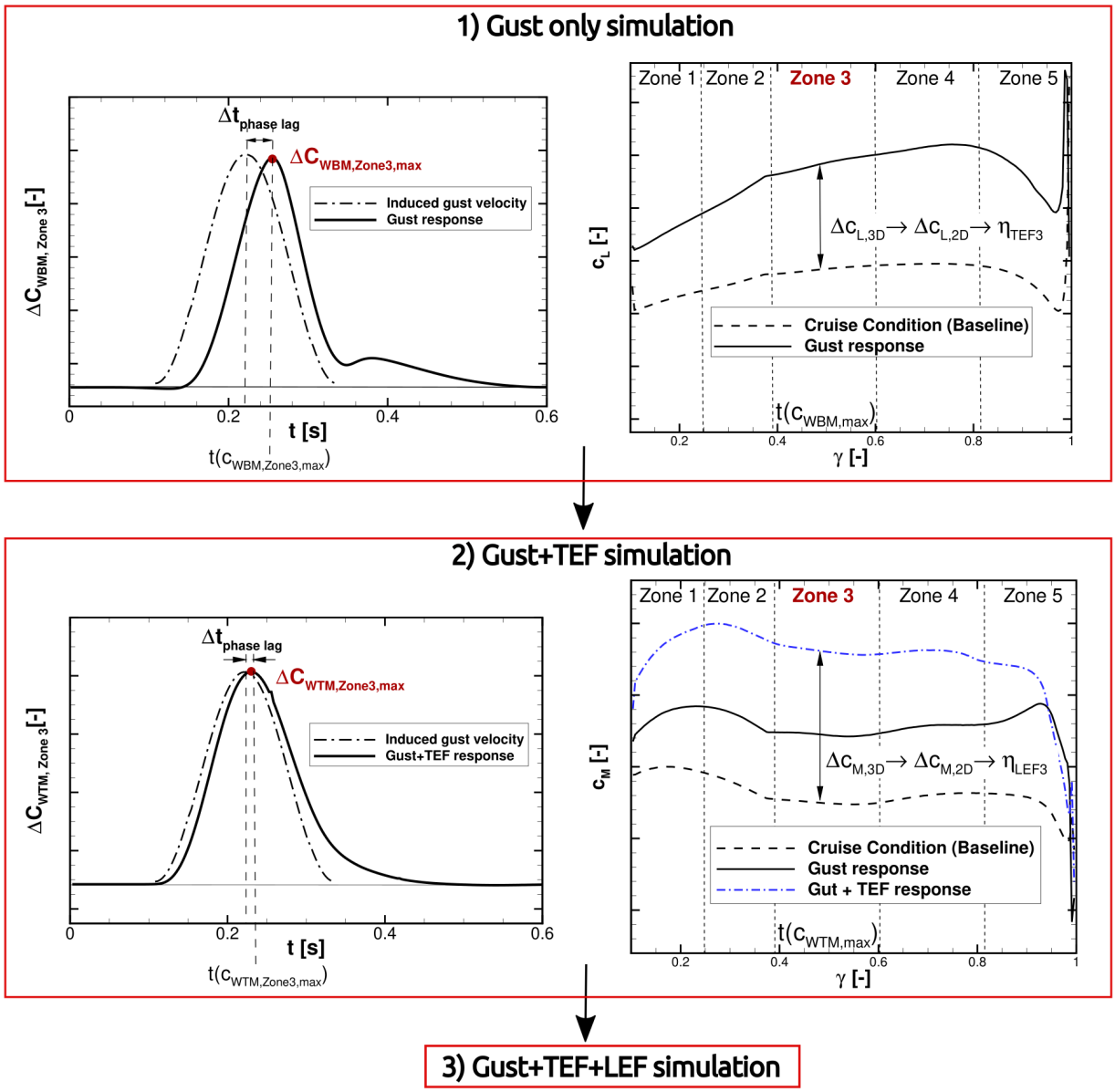

Fig. 4 Illustration of AGLA Approach with TEF and LEF deflections.

the point where the gust is introduced into the computational domain to the individual spanwise wing segments is denoted as Δt_i.

The step 2) includes dynamic TEF simulations at gust inflow conditions. This intermediate simulation step is used to identify the required LEF deflection angles as the TEF deflections itself lead to an c_M-elevation which is in the same order of magnitude as the maximum increase caused by the gust impact. The spanwise c_M distributions at the time of the maximum WTM (see Eq. (1)) as resulting from step 1) and step 2) are depicted in the bottom right plot in Fig. 4. The increase in the spanwise c_M distribution caused by TEF deflections is clearly visible. The spanwise c_M resulting from TEF deflections at gust inflow conditions at the time of the maximum WTM are compared with the reference cruise condition in zone 3 to calculate the required deflections of the LEF 3 on the 3D wing. The basis for the estimation of the 3D LEF 3 deflection amplitude is provided by the 2D LEF 3 efficiencies in $\Delta C_{M,2D}$ and the 2D-3D data transformation. The impact of the LEF deflection on the spanwise lift and consequently on the WBM is also considered, as it can not be omitted for large LEF deflections. This leads to an adjustment of the TEF deflections toward smaller angles.

3) The last set of simulations consist of dynamic TEF and LEF deflections at gust inflow conditions. The individual TEF and LEF schedulings follow the time functions derived from Eq. 6. The evaluation of the WBM and WTM time histories and the spanwise loads represent the final result for the assessment of the AGLA approach.

III. Results

A. Prestudy – Critical Gust Loads

Even though different gust prediction methods were developed in recent years to

Different methodologies have been proposed in recent years to quickly identify worst-case gust load scenarios [50, 51]. However, as the focus of the present work is on gust loads at design cruise inflow conditions, the number of required simulations to predict the critical gust scenario is manageable. All gust velocity profiles depicted in Fig. 3 were used for the prestudy on the LEISA configuration to derive the critical gust scenario. The research model is added to Fig. 3 to demonstrate its relative size compared to the gust wave lengths. The time responses of the LEISA configuration to the gust velocity profiles depicted in Fig. 3 are shown in Fig. 5. A clear saturation of the gust induced lift coefficient C_L for $\lambda_{Gust} > 80\,\mathrm{m}$ is visible. This saturation can be referred to viscous effects which initiate gust induced flow separation. It is shown in previous work [33] that the effective angle of attack is correlated to λ_{Gust} which makes aircraft flying through gusts with high λ_{Gust} prone to shock induced flow separation. Studies by Mallik et al. [52] at low speed conditions of $M = 0.2$ show that the peak C_L values are strongly dependent on the wings angle of attack. For small wave lengths in the order of $3 \times c$ the C_L peak loads appear for high angle of attack with incipient stall. However, for large wave lengths in the order of $28 \times c$ the C_L peak values of the smallest angle of attack are

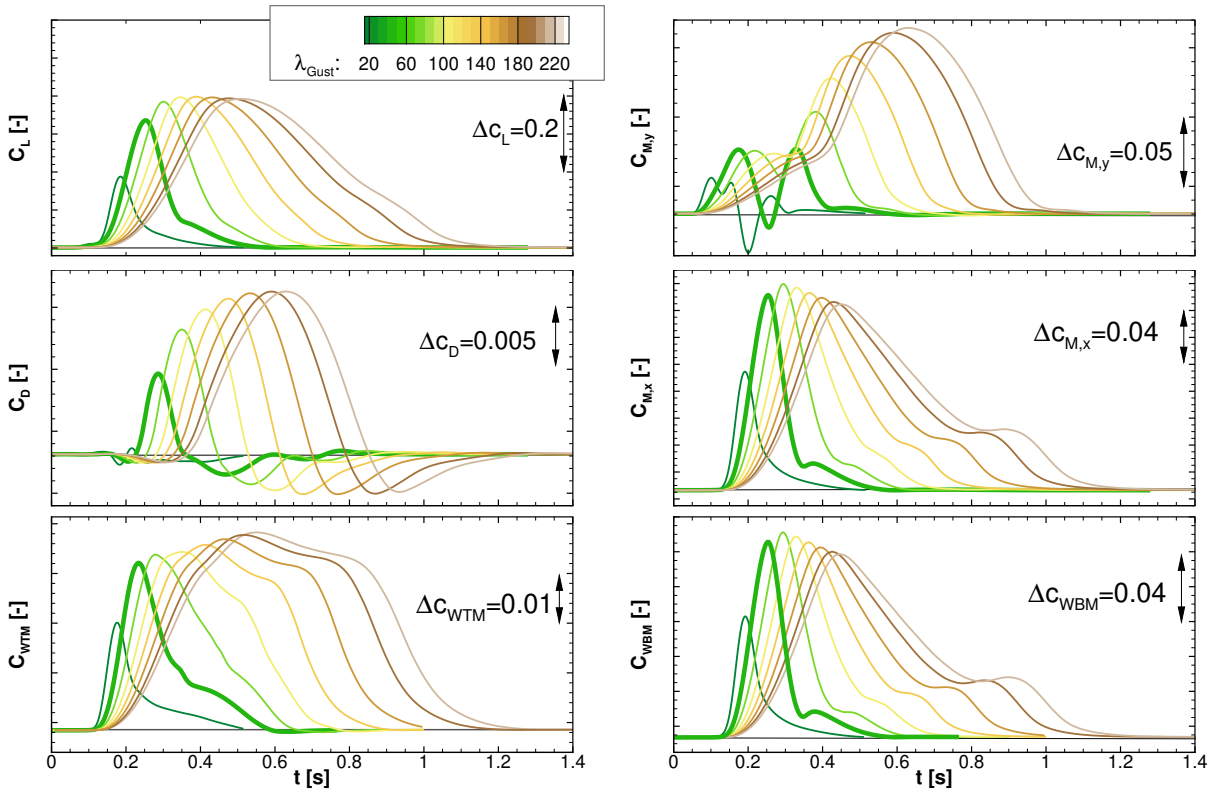

Fig. 5 Gust wavelength study on 3D configuration based on FAR25 regulations, see Fig. 3. The time histories resulting from the interaction with the reference gust (λ_{Gust} = 50 m) are highlighted by a thicker line.

significantly larger. These results of Mallik et al. [52] strengthen the assessment of the C_L-curves presented in Fig. 5. The maxima of the drag coefficient C_D increase with λ_{Gust} but again a decrease in drag rise with increasing λ_{Gust} is clearly apparent. The pitching moment coefficient $C_{M,y}$, which is computed by using the center of gravity of the LEISA aircraft as reference point, shows a maximum in $|\Delta C_{M,y}|$ for the gusts with λ_{Gust} = 220 m. Gusts with $\lambda_{Gust} \leq 110$ m show two or more local maxima with embedded minima indicating a pitch-up effect followed by a pitch-down effect on the aircraft. On the other hand, gusts with $\lambda_{Gust} \geq 110$ m lead to a nose-up effect only. The reason for the fluctuating behavior of the pitching moment for smaller λ_{Gust} is attributable to the relatively short interaction time between the peak gust velocities and the whole wing. A spanwise and chordwise variation of the gust induced velocities is more pronounced for small λ_{Gust}.

The maximum in the wing bending moment coefficient C_{WBM} occurs for λ_{Gust} = 80 m. When comparing these results with the gust wavelength study at lower U_{ds} presented in [33], besides the obvious increase in gust induced forces and moments, the time histories presented here for $\lambda_{Gust} \geq 80$ m show a clear non-linear behavior. This is attributable to shock induced flow separation and is detrimental for the efficiencies of the control surfaces. The roll moment of the aircraft $C_{M,x}$ is evaluated about the longitudinal axis of the aircraft. Therefore, when compared to C_{WBM} it includes the contribution of the fuselage besides the difference in the moment reference point. As the gust effect on the fuselage is

rather small compared to the gust effect on the wing, a direct correlation between C_{WBM} and $C_{M,x}$ can be assumed. The evaluation of wing torsional moment coefficient C_{WTM} calculated in a postprocessing step by using Eq. (1) shows that "1 − cos" gusts increase the C_{WTM} by introducing a positive (nose up) c_M along the wing span. The C_{WTM} curves demonstrates a similar behavior as the C_L curves in terms of saturation of the maximum loads with increasing λ_{Gust}. However, compared to the time histories of C_L and the C_{WBM} for $\lambda_{Gust} \geq 110\,\text{m}$, C_{WTM} remains at high levels for a longer period of time after reaching its maximum. This difference in time histories between the structural coefficients C_{WBM} and C_{WTM} of the wing may require different time functions, especially in terms of the flap actuation periods of the TEF and LEF. Control of gust induced pitching moment via pitch motion of the aircraft is roughly one order of magnitude higher than with ailerons and spoilers [53]. Furthermore, it is well known that flaps at the Horizontal Tail Plane (HTP) are far more effective than TEF on wings with regard to pitching moment control due to large lever arm to the aircraft's center of gravity. Statements on the time response of C_L are also inconclusive when neglecting flight mechanics.

In the following the time histories of the pitching moment coefficient $C_{M,y}$, the drag coefficient C_D, the lift coefficient C_L and the roll moment coefficient $C_{M,x}$ are only monitored while focus is laid on C_{WBM}, and C_{WTM}. In the last section Sec. III.D all force and moment coefficients are revived in an overall assessment of the AGLA efficiency to exclude unintended reactions to TEF and LEF deflections. The gust with a wavelength of $\lambda_{Gust} = 50\,\text{m}$ and a design gust velocity of $U_{ds} = 14.48\,\text{m/s}$ is selected as critical gust scenario as it represents a good compromise between experienced structural gust loads and computational time. The time histories of the gust simulations with $\lambda_{Gust} = 50\,\text{m}$ are highlighted through a thicker line in Fig. 5. In addition, lower frequency gusts grant more time to an aircraft for a reactive response reducing the severity of gust induced wing loads.

The contributions to C_{WBM} and C_{WTM} by the five spanwise wing zones are plotted in Fig. 6. These are essential for the extraction of the time of maximum C_{WBM} and C_{WTM} for each zone, which is further processed as outlined in Sec. II.C. Due to the small lever arm the loads on the wing zones 1 and 2 show only a minor contribution to the initial C_{WBM} level and the increase in gust induced C_{WBM}. The contribution of the zones 3-5 to the overall C_{WBM} is in the same range. While zone 5 has the largest lever arm toward the reference point at the wing root, the wing zones 3 & 4 compensate the reduced lever arm through their larger local chord lengths. A further reduction of C_{WBM} at zone 5 is caused by the tip-effect. The undershoot in C_{WBM} for the zone 4 and 5 is attributable to local flow separation and thus allows to identify the regions of separated flow as a reaction to the gust. It needs to be mentioned that our approach of AGLA does not include a full exploitation of the different contributions of the wing zones to the overall C_{WBM}. The method which aims at an elimination of the local spanwise lift increase throughout the gust event does not take into account the varying effects of the TEF along the span due to the lever arm. This means e.g. that a utilization of TEF 1 is necessary to alleviate the local spanwise c_L, however, this will only have a minor impact on the overall C_{WBM} reduction. The opposite is true for the efficiencies of the outboard TEF. This fact was deliberately neglected in this work to be

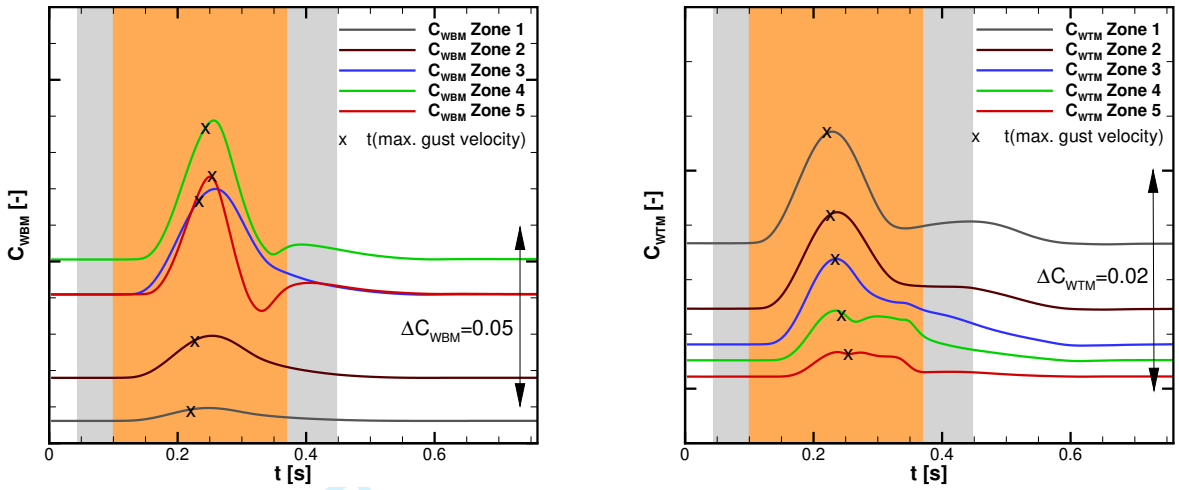

Fig. 6 Distribution of gust loads to the wing zones depicted in Fig. 1 for the reference gust with $\lambda_{Gust} = 50$ m. Orange area indicates interaction time of the gust with the wing and orange area together with the gray area indicates interaction time with the fuselage-wing configuration.

able to asses the introduced prediction method for the flap deflection amplitudes and the assumptions therein. The integration of the impact of spanwise lift variations would significantly impede a straightforward AGLA approach and devalue the mono-disciplinary CFD simulations regarding their validity. This means that there is room for improvement in terms of efficiency for C_{WBM} reduction by dynamic TEF deflections.

The C_{WTM} time histories of the wing zones show that it is independent from the lever arm, but greatly depends on the local chord length and spanwise extension of the respective wing zone. The ΔC_{WTM} decreases from the most inboard zone (zone 1) to the most outboard zone (zone 5). Flow separation at zone 4 and zone 5 leads to a lower increase in C_{WTM} and a clear divergence from the "1 − cos" type gust response. In terms of reduction of gust induced C_{WTM}, the spanwise effects of the LEF are directly applicable to the zonal C_{WTM}. Nevertheless, as the TEF deflections strongly affect the increase in the zonal C_{WTM}, a consideration of the spanwise varying TEF efficiencies with regard to the C_{WBM} reduction, has an indirect impact on the ability of the LEF to compensate the total increase in C_{WTM}. Inefficient inboard TEF deflections regarding the alleviation of C_{WBM} further increase the already high maximum in C_{WTM} and thus reduce the capacity of the inboard LEF to fully mitigate the ΔC_{WTM}. Again, the AGLA approach in the present work does not consider this deterioration of the LEF efficiencies as it is destined to study the applicability of the presented 2D-3D strip theory. Besides the identification of the times with maximum zonal C_{WBM} and C_{WTM} an additional information that is of concern is the phase shift between the maximum gust induced vertical velocity and the peak loads. The time of impingement with the maximum gust induced vertical velocity is highlighted by cross-marks on the zonal C_{WBM} and C_{WTM}. While there is a general delay in the zonal C_{WBM} reaction, except for zone 3, the peak loads of the zonal

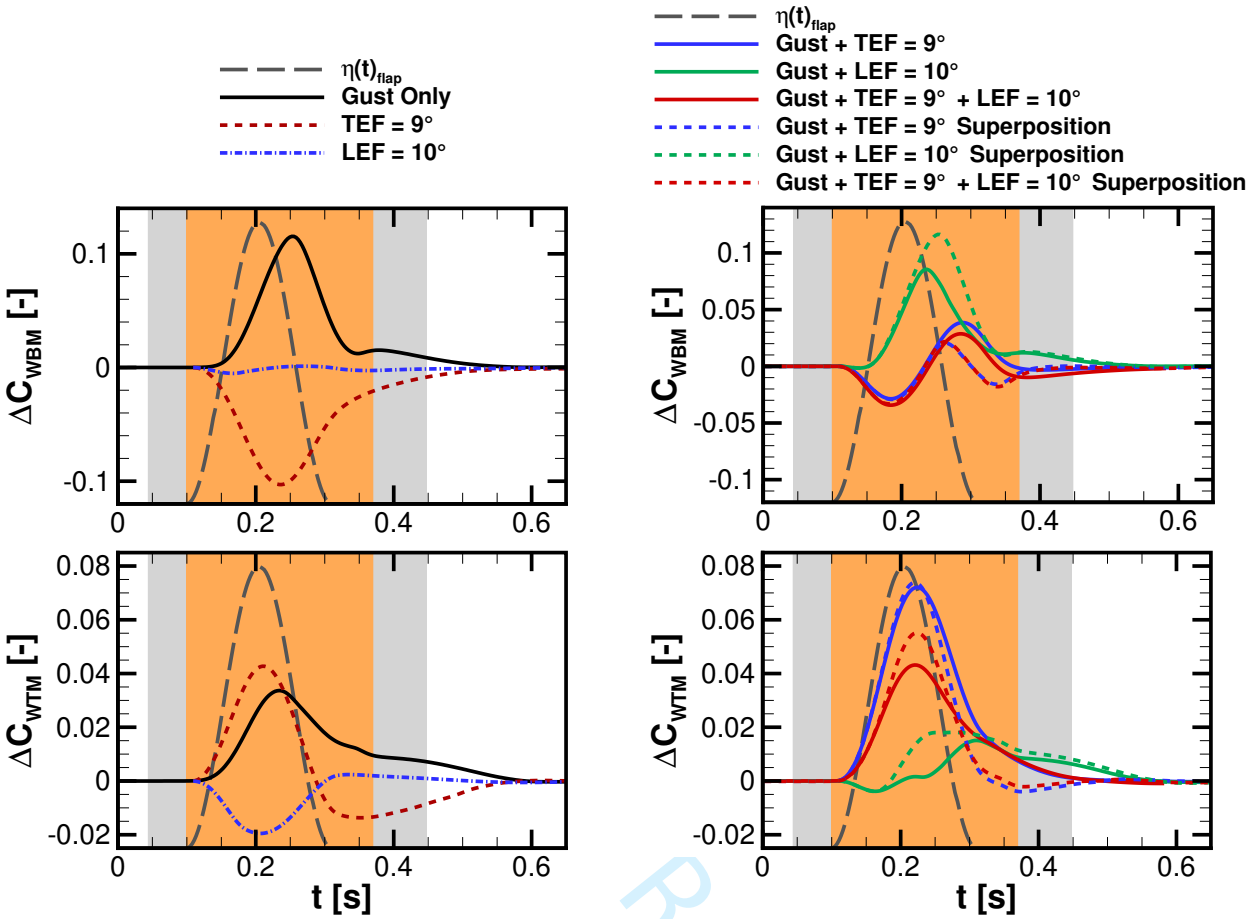

(a) Individual effects of gust, TEF and LEF (b) Superposition of effects

Fig. 7 Superposition of gust effect with TEF and LEF deflections from 3D aircraft simulations. For the description of background coloring please refer to Fig. 6.

C_{WTM} almost fall together with the maximum gust velocities. These identified phase shifts are considered by the AGLA approach as described in Sec. II.C.

B. Proof of Validity for AGLA Concept

The AGLA approach as introduced in Sec. II.C.2 assumes a transferability between 2D and 3D results of dynamic flap deflections and an ability to superimpose gust and dynamic flap effects. A thorough investigation was conducted to verify both aforementioned assumptions of which selected results will be presented next. Even though Neumann [54] has shown that the vertical loads from a periodic cosine-type gust scenario can be decomposed into the loads resulting from its elastic movement and the loads resulting from the periodic wind field, no studies are available that demonstrate the same for dynamic flap deflections at the highly unsteady flow conditions as observed in this work.

The time histories of the individual effects of the reference gust, a continuous TEF deflection of $\eta_{TEF1-5} = -9°$ and continuous LEF deflection of $\eta_{LEF1-5} = 10°$ are depicted in Fig. 7(a) along with the time history of the flap deflections

$\eta(t)_{flap}$. The results presented in Fig. 7 do not consider the geometric phase lag resulting from the wing sweep for the flap schedulings. All flaps are actuated simultaneously. The flap amplitudes are selected to be representative for the final flap amplitudes used in the final AGLA simulations with spanwise segmented TEF and LEF. As shown by the authors of the present paper in [33], a TEF deflection is suitable to counteract the gust induced WBM, however, it generates a nose up moment along the wing-span and thus adversely affects the WTM in an amplifying manner to the gust effect. A LEF deflection with $\eta_{LEF1-5} = 10°$ has no major impact on the WBM, but generates a nose down effect along the span and consequently a reduction of the gust and TEF induced WTM. Fig. 7 (b) shows the results of the combined simulations of the gust with TEF deflection, the gust with LEF deflection and the gust with TEF and LEF deflections along with the superimposed results of the individual simulations. The superposition of the gust and LEF effects and gust and TEF effects show clear discrepancies in the peak loads of C_{WBM} when compared to the combined simulation. At gust inflow conditions the downward deflecting LEF amplifies the flow separation, which is already present at the time of maximum gust induced loads. At steady or uniform inflow conditions, the LEF deflection does not introduce flow separation. On the other hand, the upward directed TEF deflection reduces the gust induced flow separation due to the decambering effect. Therefore, the combined simulations lead to smaller C_{WBM} values for the LEF deflection and to higher C_{WBM} values for the TEF deflection when compared to the superimposed results. Again, while there is no major contribution of the LEF to the C_{WBM} time history for the superimposed results of gust, TEF and LEF, the combined simulations of these three effects indicate a larger effect of the LEF deflection to the maximum C_{WBM}. While there is a quite good agreement in the peak values of C_{WTM} for the TEF deflection, deviations are visible at time values after the peak load. This is assignable to the occurrence of gust induced flow separation in this time range. For the LEF deflection larger deviations in C_{WTM} are apparent in the time range during the LEF deflection. This difference in the LEF effects on C_{WTM} is also transferred to the peak C_{WTM} of the final results of TEF and LEF deflections at gust conditions. Despite the deviations of approx. 14.3% in the peak loads of C_{WTM} and 3.9% in C_{WBM} for the final results of Gust+TEF+LEF, the results indicate a general applicability of the superposition of the three individual effect at the prevailing highly unsteady transonic conditions.

Besides an evaluation of the global wing loads an investigation of the local wing loads is essential for the proof of the ability to superimpose the effects. Coincidental chordwise and spanwise redistribution effects can lead to an interference of aerodynamic effects which lead to similar global wing loads despite being inherently different than those resulting from a superposition of the individual effects. The effects of vertical "1 − cos" gust, continuous upward deflected TEF deflections and continuous downward deflected LEF deflections on the c_p-distributions are depicted in Fig. 8. These results are also documented in [33] and are thus only shortly outlined below. The gust effect on c_p is similar to an increase in the angle of attack of the aircraft. The c_p levels exhibit a flow acceleration on the suction side of the wing and a deceleration on the pressure side of the wing. An upward directed TEF deflection shows a rise in c_p in the rear section of the suction side due to a decambering of the wing. A drop in c_p on the pressure side of

the wing in the area comprising the rear section is assignable to a reduction of the rear loading caused by the upward directed TEF deflection. On the suction side the nose down movement of the LEF leads to a decrease in the suction peak and a subsequent acceleration in the vicinity and downstream of the LEF's hinge line. The increase in c_p level in the leading edge area and the decrease in c_p level further downstream can be seen as an explanation of the rather small impact of an LEF deflection on the spanwise c_L distribution and consequently on C_{WBM}. The Δc_p on the pressure side of the wing caused by a LEF deflection shows an opposed behavior compared to effects on the suction side but with smaller magnitude. The Δc_p contours at the time of the maximum flap deflections, see $\eta(t)_{Flap}$ in Fig. 7, as resulting from combined simulations of gust, continuous TEF deflection and continuous LEF deflections and the superposition of the individual effects are depicted in Fig. 9. The Δc_p are adjusted with the baseline cruise condition. The top images of each subplot show the results from the combined simulations and the bottom images show the results from superimposing the individual effects. Overall a good agreement in the local flow structures can be observed when comparing the superimposed results with the results from the combined simulations. This is true for the superposition of the gust with the individual TEF and LEF deflections as shown in Fig. 9(a)&(b) as well as for the superposition of all three effects as shown in Fig. 9(c). The stronger acceleration in the superimposed results with LEF deflection 9(a)&(b) downstream of the LEF hinge line are attributable to the above mentioned lack of reproducibility of flow separation at steady inflow conditions.

A proof of the transferability of the 2D simulations is discussed next. The spanwise lift and pitching moment distributions from the 3D simulations of individual and continuous TEF and LEF deflections and the related 2D data points are depicted in Fig. 10 at the time of the maximum loads. The spanwise distributions of the baseline cruise

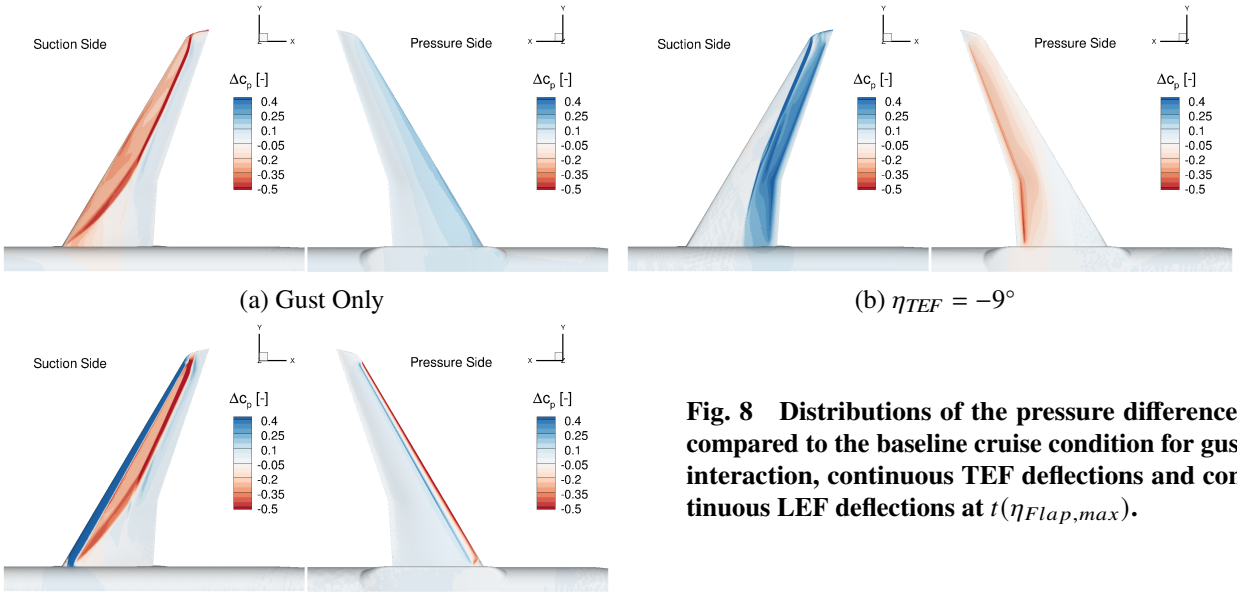

(a) Gust Only

(b) $\eta_{TEF} = -9°$

(c) $\eta_{LEF} = -10°$

Fig. 8 Distributions of the pressure differences compared to the baseline cruise condition for gust interaction, continuous TEF deflections and continuous LEF deflections at $t(\eta_{Flap,max})$.

condition are added as reference. The subplots (a) and (b) in Fig. 10 show in an exemplary way the results of individual and continuous upward directed TEF deflections at $-7°$ and the subplots (c) and (d) show the results of individual and continuous downward directed LEF deflections at $-8°$. The 2D data are extracted from simulations with flap deflections η corrected according to Eq. (4). While the 2D data for c_L represent the absolute values from the 2D simulations, the depicted 2D data for c_M are calculated by adding the Δc_M to the baseline results of the 3D simulations. This step allows to diminish the differences between the baseline results of the 2D and 3D setups for the pitching moment coefficients, where no alignment was performed between the 2D and 3D baseline conditions. The results of the individual 3D TEF deflections show that their effects clearly exceed their spanwise geometrical extension. This is true especially for the individual TEF deflections at the inboard wing, where the disturbance caused by the TEF is propagated in spanwise direction because of the backward directed sweep of the wing. The effect on the local c_L

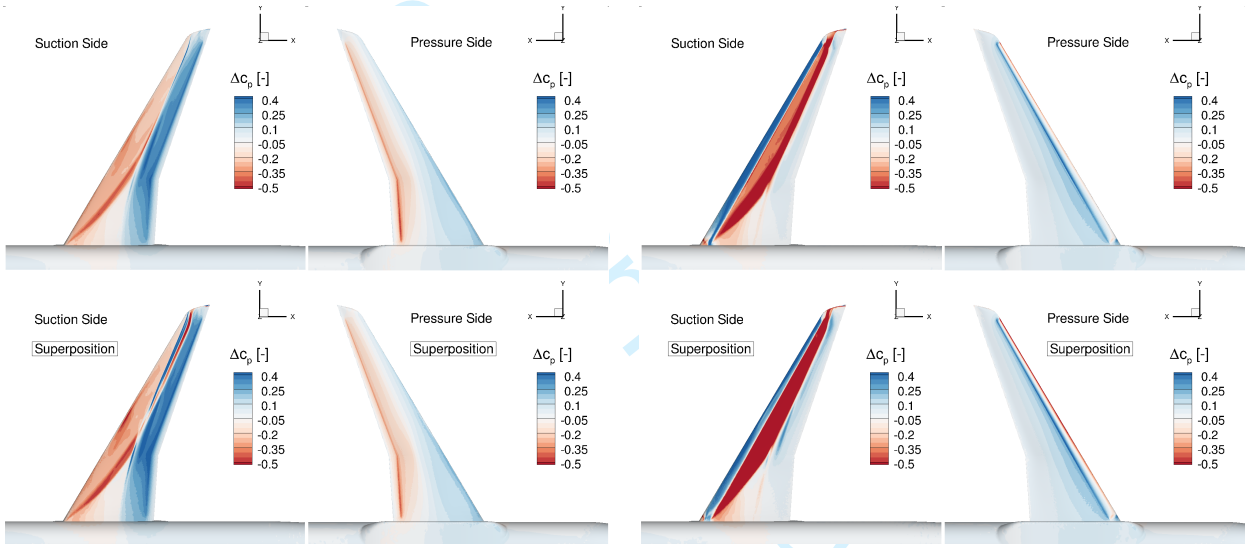

(a) Gust + $\eta_{TEF1-5} = -9°$

(b) Gust + $\eta_{LEF1-5} = -10°$

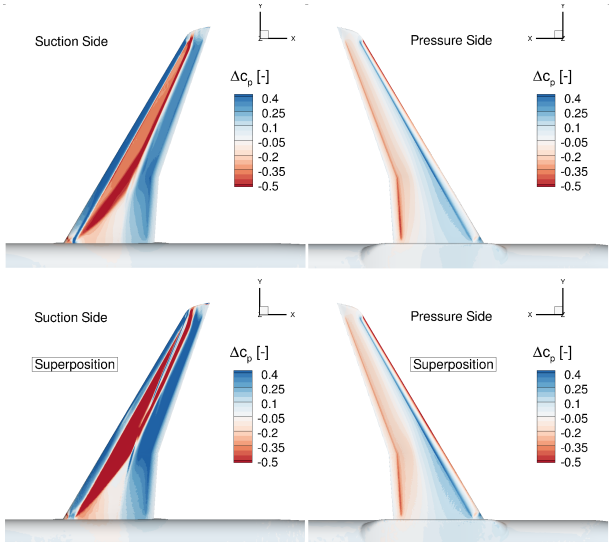

(c) Gust + $\eta_{TEF1-5} = -9°$ + $\eta_{LEF1-5} = -10°$

Fig. 9 Distributions of the pressure differences compared to the baseline flow at $\eta(t)_{Flap,max}$ resulting from simulations of combined gust & continuous TEF deflection, gust & continuous LEF deflection and gust & continuous TEF & LEF deflections. Top images of each subplot show the results from the combined simulations and bottom images show the results from superimposing the individual effects shown in Fig. 8.

by individual or discrete TEF deflections is far smaller than predicted by the 2D simulations. A far better agreement between 2D and 3D data can be achieved by the continuous TEF deflection. The reduced efficiency of individual TEF deflections compared to continuous TEF deflections is attributable to the secondary aerodynamic effects of trailing vortices. The vortex system associated with 3D flap deflections consist of trailing vortices and shed vortices. Temporal changes in bound circulation initiated by e.g. TEF deflections create transverse wake vortices which are called shed vortices. The re-induced velocities of these shed vortices and the related change in the effective angle of attack and consequently wing loads is captured by the 2D and 3D simulations in the same way. This is not the case with trailing vortices which can not be captured by 2D simulations. Trailing vortices are based on spatial circulation conservation and originate from the gradient of bound circulation along the wing span. An upward deflected TEF reduces the bound circulation in the TEF section and high gradients develop at the flap edges. The flap edge vortices proceed in flow direction. According to Biot-Savart's law these vortices create an upwash in the flap section and a downwash in the adjacent wing section which is the main reason for the large deviation of the 3D c_L of the discrete flap deflections to the 2D data. The deviation between the c_L from the continuous TEF deflections and the 2D data in the root region is attributable to 3D root effects and the rather large deviation of the inboard wing planform from a swept wing geometry. Despite the presence of 3D tip effects the agreement in c_L between 2D data and continuous 3D TEF deflections at zone 5 is quite good. A method to cover the tip effects, the root effects and the deterioration of the 2D-3D transformation at the inboard wing will be introduced as an extension in Sec. III.E. The computationally expensive 3D results of individual TEF deflections illustrate their incapability to provide an appropriate assumption for 3D flap deflections with similar amplitudes along the span. The agreement between 2D data and 3D data in the spanwise c_M is also improved when considering continuous 3D TEF deflections. A correction for the 2D TEF efficiencies to enable representative efficiencies for discrete 3D TEF deflections requires a consideration of the effects caused by the trailing vortices. The effect of discrete TEF deflections on the bound circulation can be derived from individual 3D simulations. However, no simple theory is known for multiple swept and tapered wings which allows to compute the induced angle of attack along the wing span resulting from a change in the bound circulation. As the final simulations with segmented TEF deflections for AGLA use similar TEF deflection amplitudes along the span the 2D database is proven to be a sound basis to estimate the 3D TEF efficiencies regarding local lift reduction. Therefore, no further efforts are made to correct the 2D database for a representation of discrete flap deflections. Additional reflections in this area are required to improve the 2D prediction in case TEF deflections along the span differ significantly.

The 3D LEF deflections show no visible impact on the spanwise c_L. The 2D data predicts a somewhat stronger impact along the full span. As the individual 3D LEF deflections show no major impact on c_L there is no change in the bound circulation and in turn no development of flap edge vortices. This leads to the good agreement in Δc_L and Δc_M between the continuous and individual LEF deflections. Except for the LEF deflection in zone 1 the 2D LEF data predict a too high impact on c_M with increasing deviation to the 3D data in spanwise direction.

The reference chord c_{ref} for the normalization of C_{WBM} and C_{WTM} is located at approx. 51% wing span, see Sec. II.A. Therefore, as the aerodynamic coefficients of c_L and c_M depicted in Fig. 10 are normalized with the local chord length the deviations between the 2D and 3D data on the outboard wing and inboard wing are not fully representative for the impact on the integral values of C_{WBM} and C_{WTM}. Furthermore, for the impact of the deviations between the 2D and 3D spanwise c_L on C_{WBM} the spanwise lever arm needs to be considered.

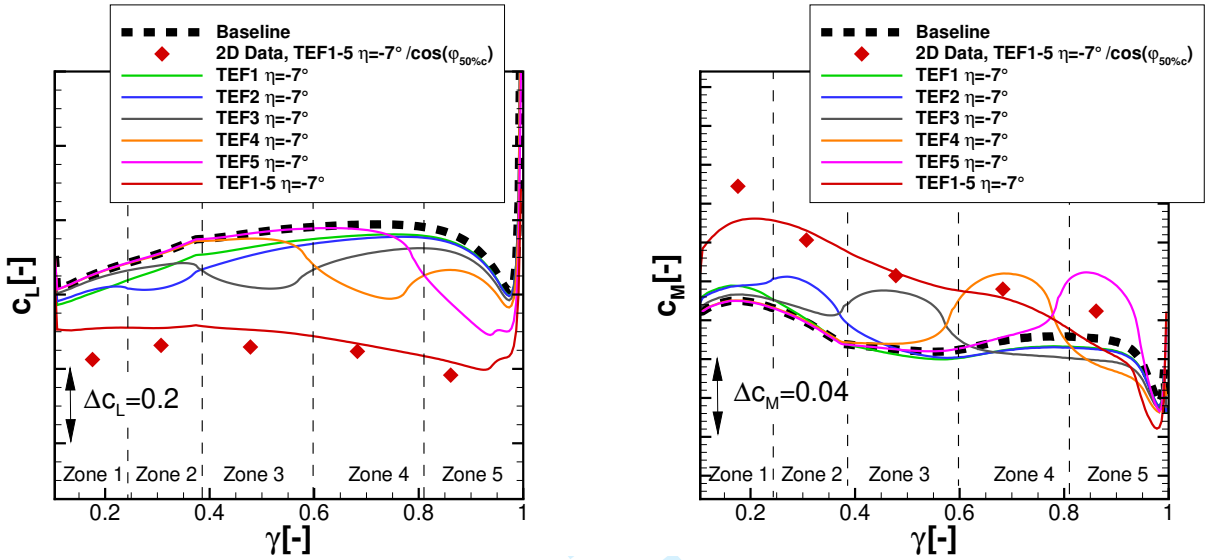

(a) Spanwise c_L and c_M for $\eta_{TEF} = -7°$ at $t(C_{WBM,max})$ and 2D data at $t(c_{L,max})$

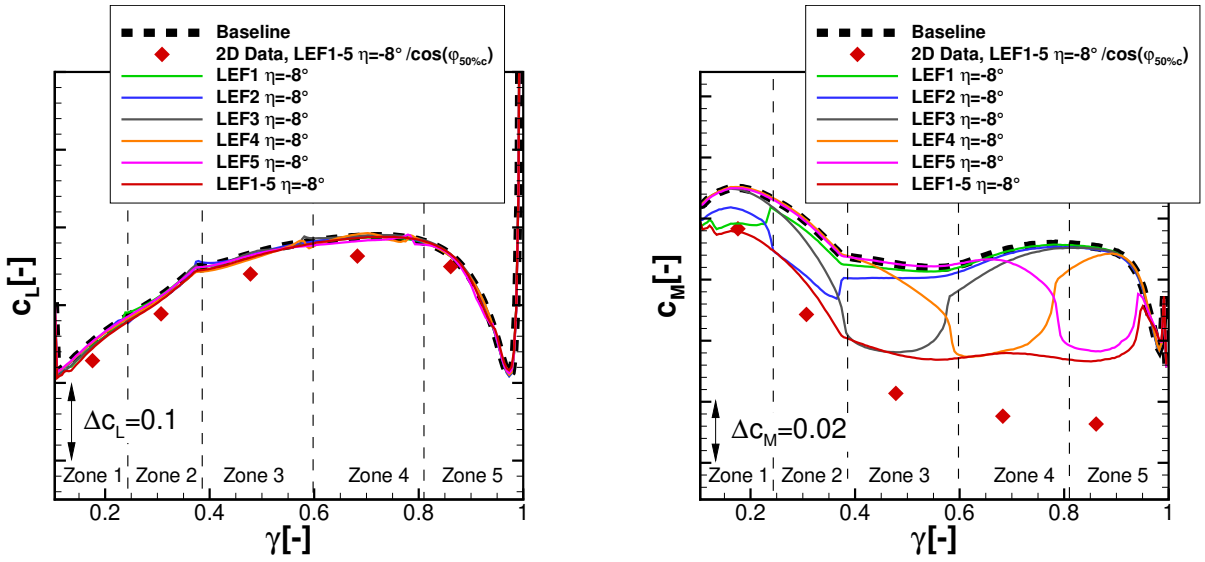

(b) Spanwise c_L and c_M for $\eta_{LEF} = -8°$ at $t(C_{WTM,max})$ and 2D data at $t(c_{M,max})$

Fig. 10 Illustration of instantaneous spanwise load distributions from 2D and 3D simulations of TEF and LEF deflections . 3D data comprises segmented and continuous TEF and LEF deflections.

C. AGLA by segmented dynamic TEF and LEF

The 2D database as extracted from the dynamic TEF and LEF simulations at the five representative airfoil sections forms the basis of the AGLA process. The starting condition for the dynamic flap simulations at the airfoils is the 2D baseline flow which is determined by Eq. (4) and the available 3D baseline flow. A "1 − cos" time function is selected as 2D flap scheduling and the time period is based on the reference gust wave length derived from the gust prestudy. A transformation of the reference gust wave length is applied by considering 2.5D wing sweep theory. The TEF are deflected in the range between $\eta_{TEF,max} = -2°\text{-} -12°$ in steps of $\Delta\eta_{TEF,max} = 2°$ and the LEF are deflected in the range between $\eta_{LEF,max} = -2°\text{-} -24°$ in steps of $\Delta\eta_{LEF,max} = 2°$. The maximum deflection amplitudes of the 2D TEF and LEF are derived from preliminary estimations of continuous flap efficiencies on the LEISA configuration [33] and a comparison with the gust loads. The maximum lift coefficients Δc_L and maximum pitching moment coefficients Δc_M at each airfoil section are depicted in Fig. 11 for a variation of dynamic TEF and LEF deflections. Fig. 11 (a) and (b) present the efficiencies of the TEF deflections regarding the impact on c_L and c_M. Besides the decrease in Δc_L with decreasing upward directed flap deflections an increase in the TEF efficiencies from the inboard section toward the outboard section is apparent. This is ascribable to the increasing relative chordwise extensions of the TEF from the wing root to the wing tip. Positive downward directed TEF deflections are included into the 2D database for a better determination of the TEF efficiency gradients $(\Delta c_L)/(\Delta\eta_{TEF})$ and $(\Delta c_M)/(\Delta\eta_{TEF})$ at small η_{TEF}, which are used in an extended approach (see Sec. III.E) to improve the mitigation of the gust loads. The Δc_M for the negative TEF deflections show an increasing nose up moment from the outboard wing towards the wing root despite the smaller relative chord lengths of the TEF at the inboard sections. This is attributable to a higher lever arm towards the 45% c line at the inboard wing sections. Fig. 11 (c) and (d) show the efficiencies of the LEF deflections. When compared to the TEF deflections, moderate LEF deflections do not contribute significantly to Δc_L, however, a major contribution can be observed at the outboard sections at high deflection angles. The major impact of the downward LEF deflections is imposed on Δc_M. In contrast to the TEF effect on Δc_M the LEF effect generally increases from the wing root to the tip, as the effect of the local chordwise LEF extension exceed the one of the lever arm.

The phase shifts introduced by the TEF and LEF deflections are also extracted from the parametric 2D airfoil simulations. Fig. 12 illustrates the temporal offsets between the maximum Δc_L and maximum Δc_M and the maximum flap deflections. The phase shift in the peak loads is normalized with the flap actuation period. A delayed reaction in $c_{L,max}$ of $\Delta t_{peak}/t_{actuation\,period} = 0.1\text{-}0.2$ is visible for the TEF deflections as shown in Fig. 12(a). This is in the order of the phase lags in C_{WBM} experienced at the wing zones by the gust encounter, see Fig. 6. These two types of phase lags oppose each other when predicting the time scheduling of the TEF. The LEF introduces only minor phase lags on $c_{M,max}$, see Fig. 12 (d). These small phase shifts in $c_{M,max}$ corresponds to the effect of the gust on the zonal C_{WTM} as marked in Fig. 6. Therefore, comparable results in terms of TEF and LEF effects can be obtained by a simple consideration of the geometric phase lag due to the wing's leading edge sweep. The phase lag in $c_{M,max}$ introduced by

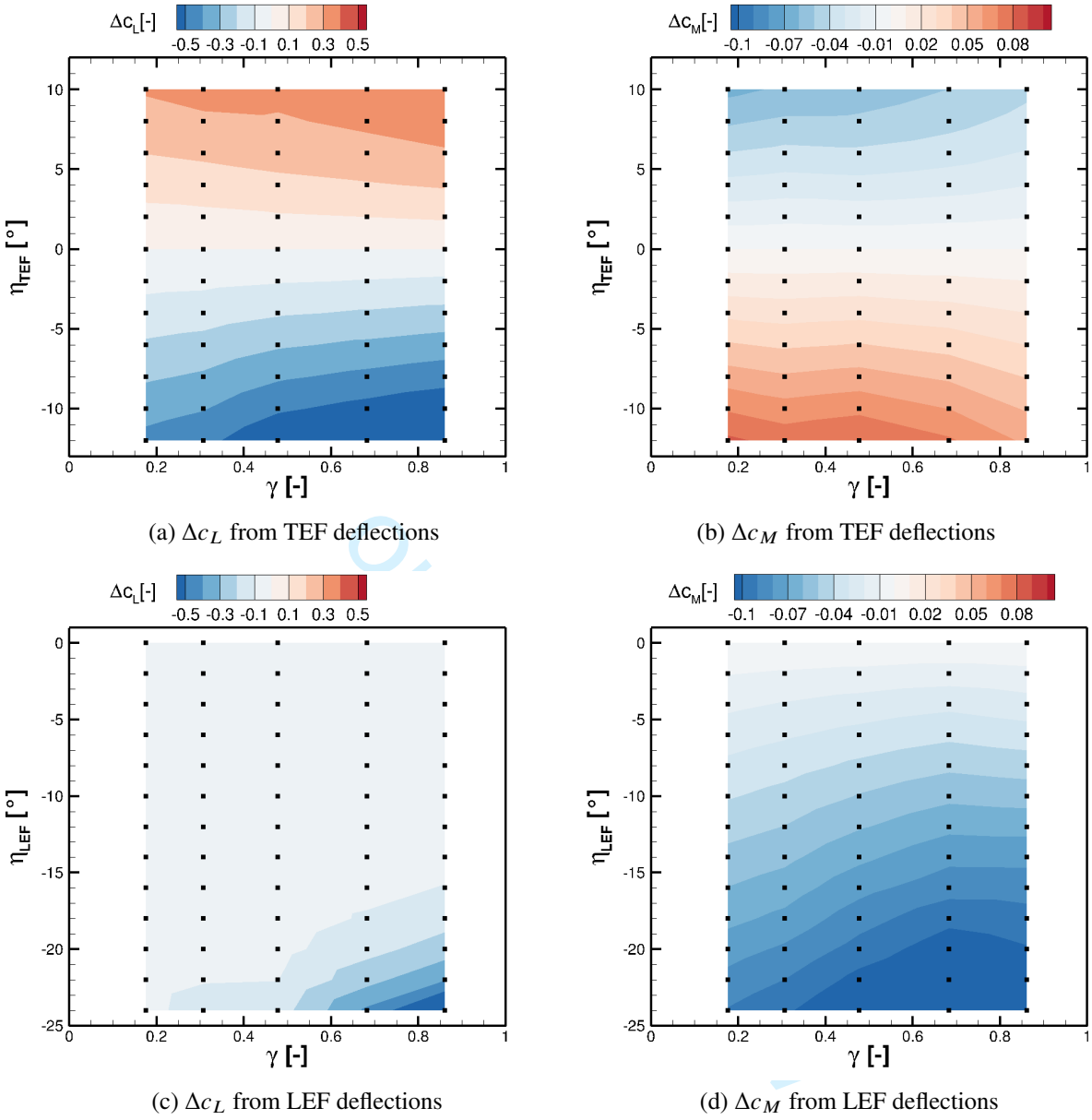

(a) Δc_L from TEF deflections

(b) Δc_M from TEF deflections

(c) Δc_L from LEF deflections

(d) Δc_M from LEF deflections

Fig. 11 TEF and LEF efficiencies from 2D database.

dynamic TEF deflections and the phase lag in $c_{L,max}$ introduced by dynamic LEF deflections are not considered in the presented AGLA approach. The large LEF induced phase lags in $c_{L,max}$ are not of concern due to the small effect of the LEF deflections on the $\Delta c_{L,max}$. The phase lag between the lift response and the flap deflection is linked to the effects of shed wake vorticity. Even though apparent mass effects might be present as well at the investigated flap deflection rates which correspond to reduced frequencies $k = \omega c/(2U_\infty)$ of $k = 0.14 - 0.42$, the main effect on the phase shift is still caused by the transverse wake vortices [55]. The values for phase lags introduced by the TEF deflections in the present work do also comply with the phase lags introduced by harmonic trailing edge flap oscillations at similar

flow conditions but 50% c chordwise extension presented by Leishman in [55]. For reduced frequencies in the range of $k = 0.14 - 0.42$ the phase of lift is 30°-37° which is conform to a phase lag of approx. $\Delta t_{peak}/t_{actuation\ period} = 0.1$.

In case of upward deflected TEF the shed vortices induce an upwind as they rotate with opposed sense of rotation to the TEF due to conservation of circulation. The effects of the shed wake vorticity exhibits a phase lag which is highly dependent on the reduced frequency, the inflow Mach number and compressibility effects [55]. As the dynamic LEF does not impose a significant impact on the lift response and thus on the bound circulation, no appreciable shed vortices are generated by an LEF deflection. This lack in shed vortices can be seen as the reason for the rather small phase shifts in the moment response resulting from LEF deflections, see Fig. 12(d).

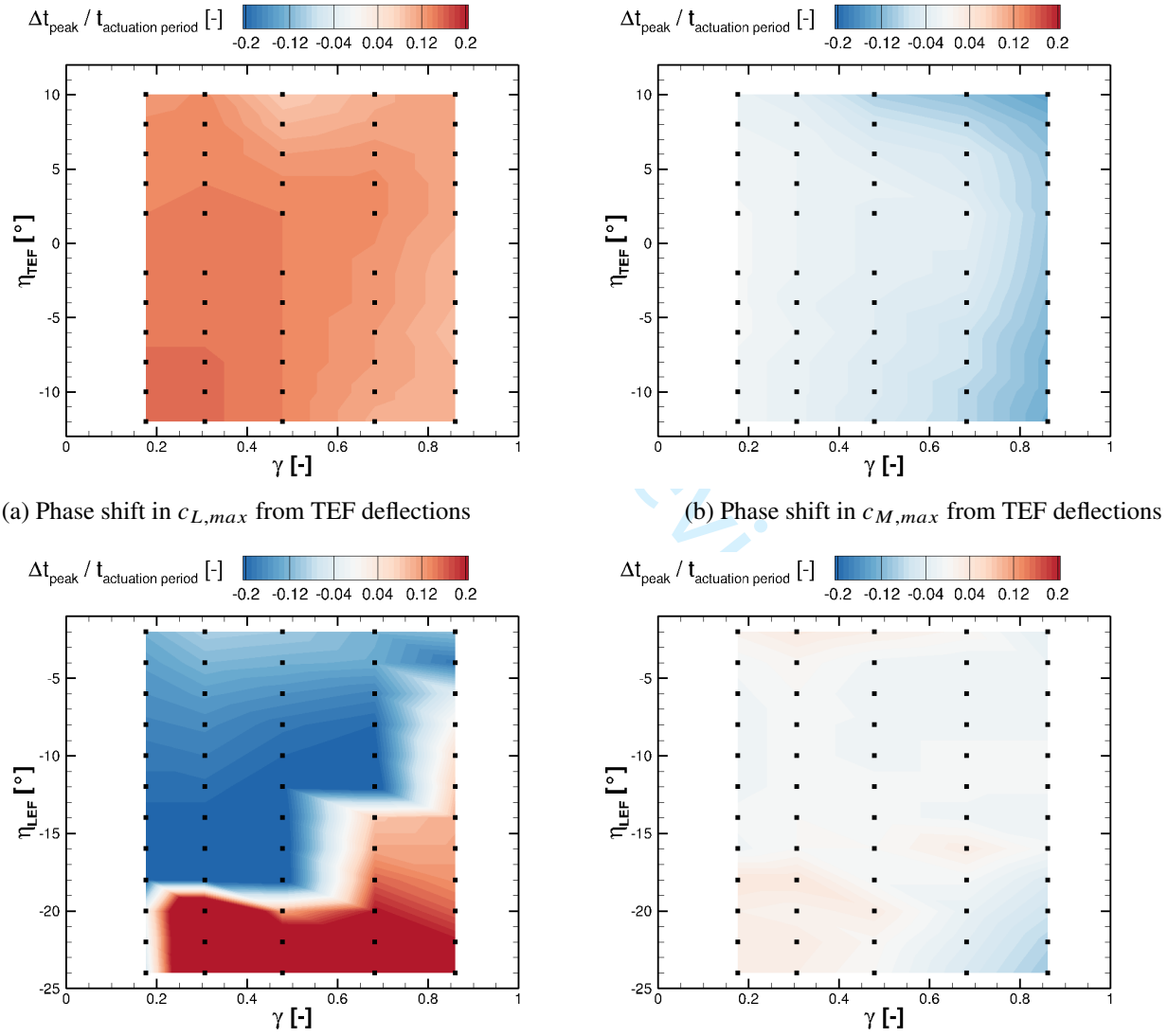

(a) Phase shift in $c_{L,max}$ from TEF deflections

(b) Phase shift in $c_{M,max}$ from TEF deflections

(c) Phase shift in $c_{L,max}$ from LEF deflections

(d) Phase shift in $c_{M,max}$ from LEF deflections

Fig. 12 Phase lags in TEF and LEF effects on $c_{L,max}$ and $c_{M,max}$ from 2D database.

The time histories of all investigated force and moment coefficients for the AGLA simulations are depicted in Fig. 13. The results of the gust simulations without deployed flaps are added as reference for the assessment of the AGLA efficiencies. Table 1 summarizes the final TEF and LEF angles utilized for AGLA. As introduced in Sec. II.C, the simulations are conducted in a consecutive manner, by first deploying the TEF only and subsequently the TEF and LEF. The estimation based on the 2D studies provide minimum and maximum deflections of the TEF of $\eta_{TEF} = -7.8°$ and $\eta_{TEF} = -9.2°$, respectively. The upward deflected TEF lead to a significant reduction in C_{WBM} which correlates with C_L. On the other hand, the TEF deflections induce a significant increase in C_{WTM}. To counterbalance the effect of the TEF and the gust on C_{WTM}, the LEF deflections are estimated based on the 2D database. As already demonstrated by the authors of the present paper in [32, 33], a full control authority of the wing torsional moment is not feasible by the presented approach with dynamic TEF and LEF. A complete compensation of the WTM loads requires LEF deflections up to 29°, see second data line in Table 1. LEF deflections of this amplitude trigger massive flow separation which leads to a highly unsteady behavior of the wing loads. This is clearly visible when analyzing the time histories of C_{WBM} and C_L for this dataset without η_{LEF} limitation. A significant overshoot and undershoot relative to the cruise condition occurs which negatively affects the LEF efficiency regarding alleviation of gust and TEF induced WTM. Furthermore, LEF deflections larger than 20° contribute significantly to a decrease in the spanwise Δc_L which distorts the prediction of the final TEF deflections based on 2D calculations. This is especially apparent for TEF where a positive or downward directed TEF deflection of $\eta_{TEF} = +0.5°$ is required to compensate the effect of the high LEF deflection. Therefore, in this work we aim at a mitigation of the adverse TEF effect on the WTM by accepting the increase in gust induced WTM. A further reduction of gust induced torsional loads requires the additional consideration of load redistribution. This can be realized by pre-deflected steady flaps as presented in [32] or during the gust interaction by adapting the dynamic flap deflections The LEF deflection angles as they result with this new approach of limited LEF deflections lead to a maximum in η_{LEF} of 16.8°, see third data line in Table 1. The limited LEF deflections still affect the TEF deflections noticeably, however the control of the spanwise C_L and thus C_{WBM} is predominantly determined by the TEF deflections. The time histories as they result with limited LEF deflections show an impact of the LEF deflections on C_{WBM}, which is manly discernible in a reduction of the overshoot. The impact of the limited LEF deflections on C_{WTM} is on the order of magnitude as intended. Despite the highly unsteady flow phenomena the clear reduction of C_{WBM} toward the standard cruise level and C_{WTM} toward the level imposed by the gust reveal a good applicability of the

Table 1 Overview of flap deflection angles η.

Case	η_{TEF1}	η_{TEF2}	η_{TEF3}	η_{TEF4}	η_{TEF5}	η_{LEF1}	η_{LEF2}	η_{LEF3}	η_{LEF4}	η_{LEF5}
TEF Only	-7.8°	-9.2°	-9.1°	-9.2°	-8°	0°	0°	0°	0°	0°
TEF + LEF w/o η_{LEF} limitation	-5.6°	-1.3°	-3.9°	+0.5°	-2.8°	24.6°	29°	25.5°	23.6°	19.1°
TEF + LEF with η_{LEF} limitation	-6.7°	-8.0°	-8.2°	-8.6°	-7.7°	13.7°	16.8°	13.1°	10.1°	6.1°

presented AGLA approach. The impact of the TEF and LEF deflections on all force and moment coefficients depicted in Fig. 13 is postponed to the final result section of the present paper (Sec. III.D).

A breakdown of the TEF effects and the combined effects of TEF and limited LEF on the zonal C_{WBM} and C_{WTM} are depicted in Fig. 14 and 15, respectively. The zonal results obtained by the gust simulations are plotted as reference. At all wing zones a nearly optimal alignment of C_{WBM} toward the cruise value is achieved through spanwise segmented TEF deflections. The unsteady overshoot and undershoot characteristics are stronger at the outboard wing which is prone to flow separation. The unsteady behavior in C_{WBM} on the outboard wing is intensified by including LEF deflections. The impact of the TEF deflections on C_{WTM} is dominant on the three inboard zones, which is due to the higher lever arm of the TEF force toward the 45% c line. The major amplification of the peak loads in C_{WTM} due to deflections of TEF 1 and TEF 2 is definitely diminishable. This can be achieved, as mentioned above, by reducing the rather inefficient TEF deflections in the inboard area and increasing the TEF deflections at the outboard wing. The evaluation of the zonal C_{WTM} for combined TEF and LEF deflections reveals a reasonable match in the peak loads at the inboard wing

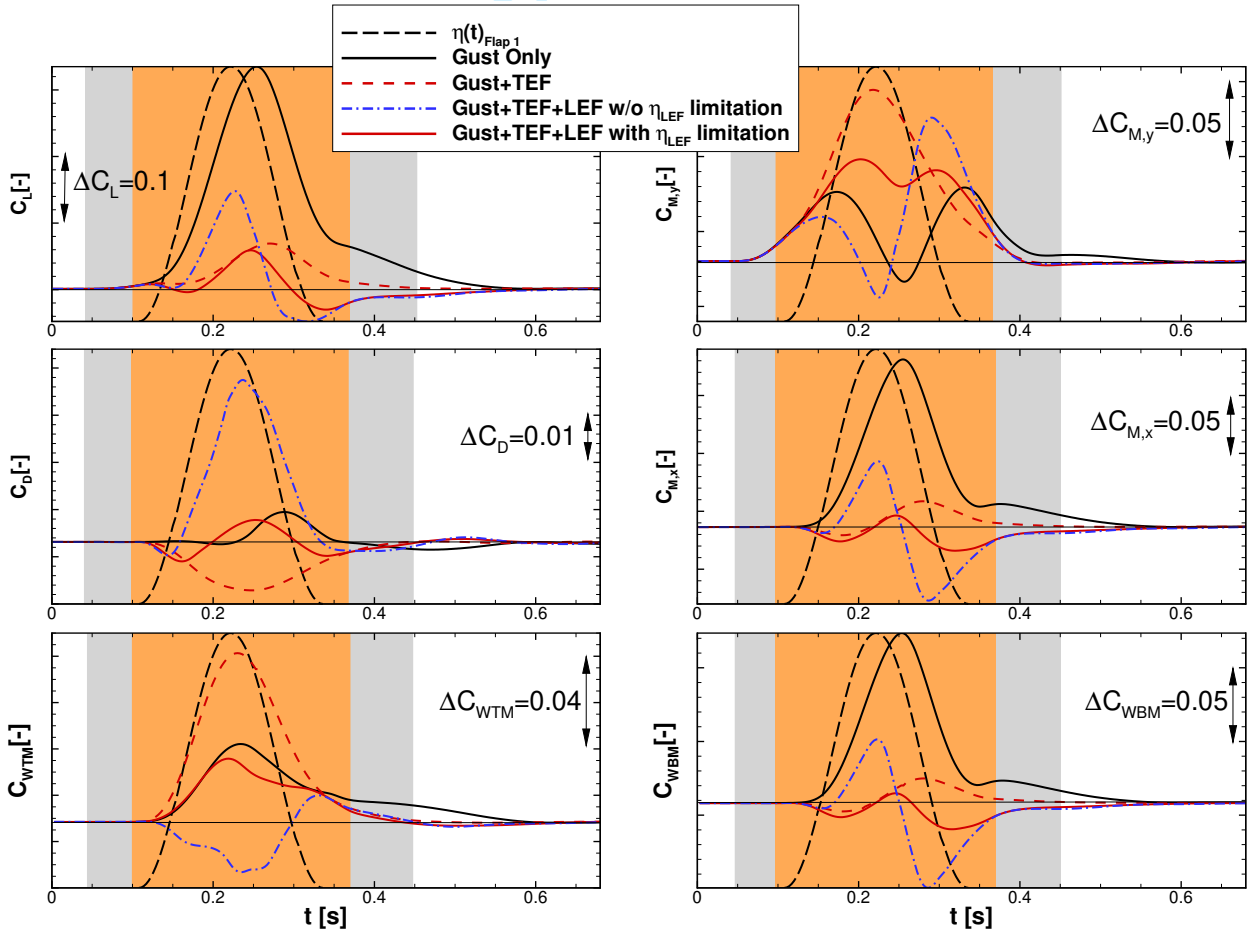

Fig. 13 Time histories of all force and moment coefficients for the LEISA configuration during gust encounter with and without AGLA. For the description of background coloring please refer to Fig. 6.

(zones 1&2). An amplification of the already prevailing flow separation impedes the aspired alignment between the peak C_{WTM} induced by the gust and the peak C_{WTM} resulting from deployed TEF and LEF deflections at the zones 3&4. Instantaneous spanwise distributions of c_L and c_M for the cases discussed above are depicted in Fig. 16 (a) and (b). The spanwise c_L and c_M are extracted at the time of the maximum c_{WBM} and maximum c_{WTM}, respectively. An exception is made for the results obtained by unlimited LEF deflections, where the spanwise loads are taken at the time of minimum c_{WBM} and c_{WTM}. This allows to detect the wing regions which lead to the pronounced undershoots in the c_{WBM} and c_{WTM} time histories for this case. For the best assessment of the AGLA method an evaluation of the spanwise load distributions at each zone for different points in time would be necessary which is not representative to an instantaneous load scenario. The simulations with only deflected TEF show some deviations in the spanwise c_L to the baseline condition. The positive Δc_L is conform to the finding of Sec. III.B, where it was shown that the TEF deflections at gust inflow condition reduce the flow separation which can not be accurately predicted by 2D TEF simulations at uniform inflow conditions. A nearly uniform increase in c_M along the wing span equipped with flaps is introduced by the TEF deflections. The inclusion of the LEF with unlimited deflection angle shows a significant drop in c_L outboard from $\gamma = 0.4$ which is linked to large scale flow separation. This flow separation leads to a significant decrease in c_M, which, despite the instantaneous benefit, introduces highly unsteady flow characteristics as illustrated in Fig. 13. When compared to the TEF only results, the results of TEF deflections overlayed with limited LEF deflections show an improved agreement in c_L at the outboard wing, while the inboard wing is adversely affected. The drop of c_L at the outboard wing introduced by limited LEF deflections can be linked to the amplification of the flow separation which is already present at gust interaction without deployed flaps. As proven in Sec. III.B, the 2D LEF simulations at uniform inflow conditions are unable to cover this effect. In case of the limited LEF deflections the c_M distributions of

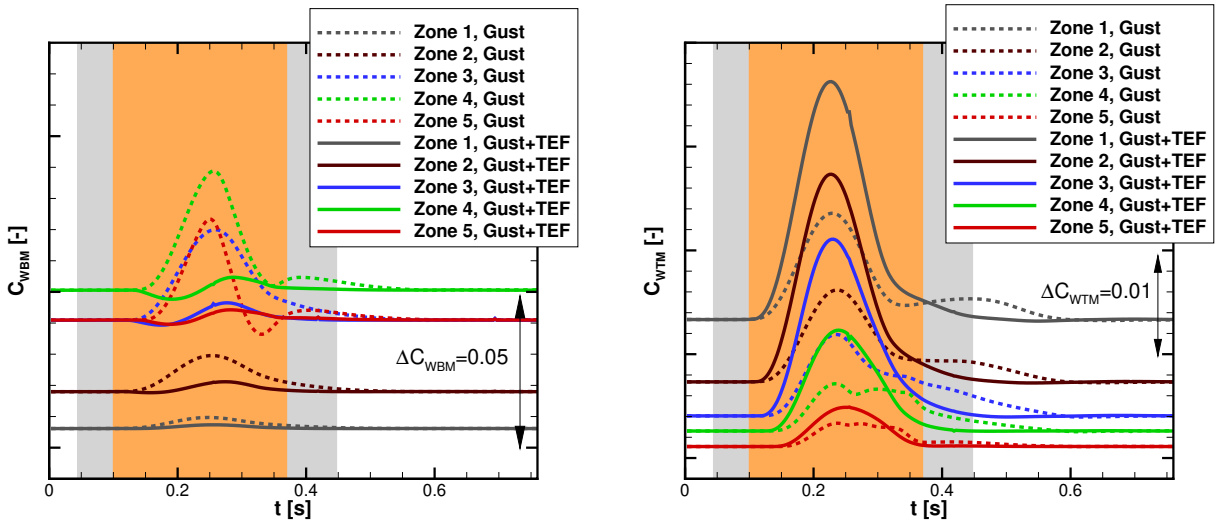

Fig. 14 Comparison of gust loads on wing zones with AGLA by TEF deflections only. For the description of background coloring please refer to Fig. 6.

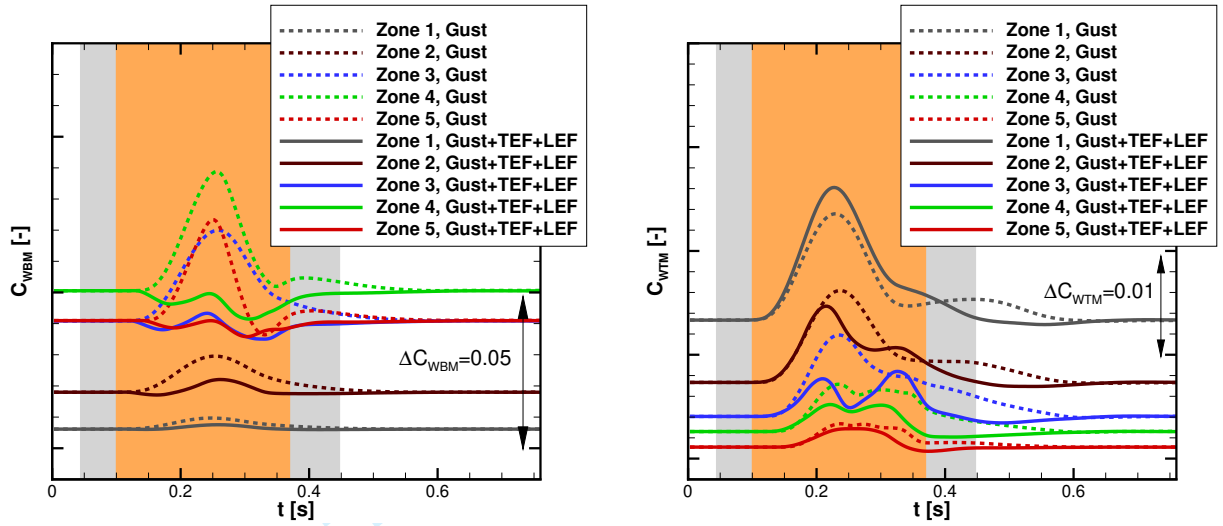

Fig. 15 Comparison of gust loads on wing zones with AGLA by TEF and limited LEF deflections. For the description of background coloring please refer to Fig. 6.

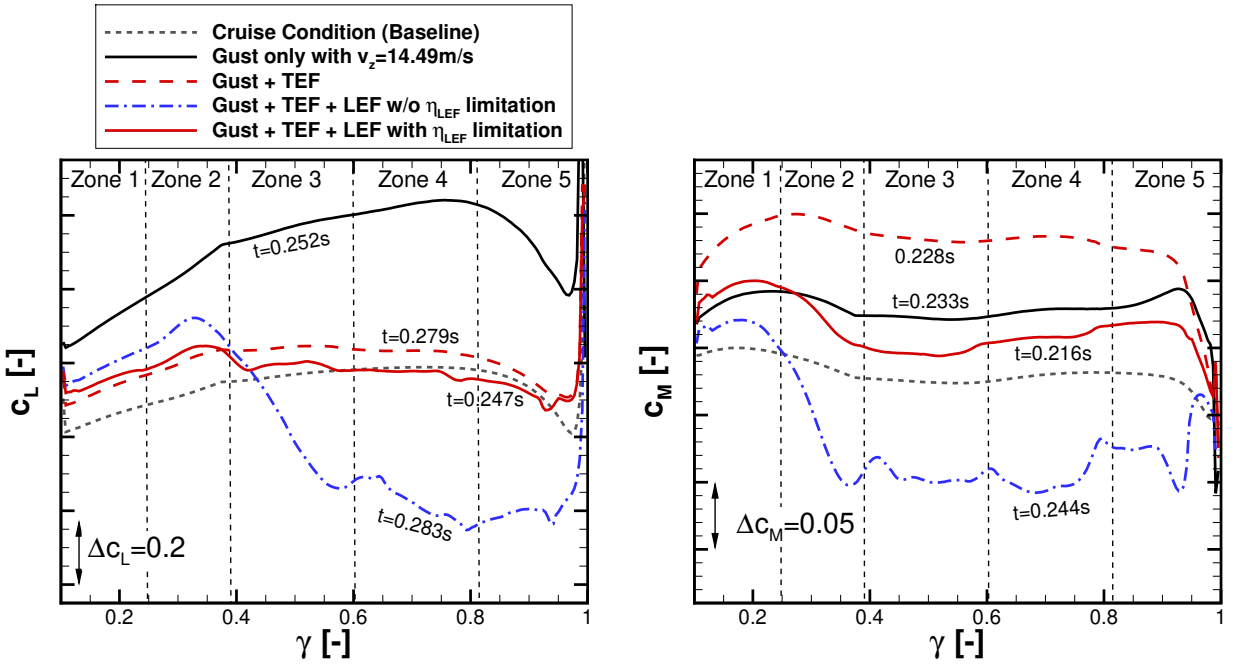

(a) Spanwise lift coefficient at $t(C_{WBM,max})$ (b) Spanwise pitching moment coefficient at $t(C_{WTM,max})$

Fig. 16 Spanwise loads resulting from gust interaction with and without AGLA.

the gust only simulations represent the target curve. A positive Δc_M in zone 1 and a negative Δc_M outboard from zone 1 is visible. The negative Δc_M is also ascribable to the prediction errors associated with the superposition of the 2D LEF simulations with the gust only simulations. Besides the errors introduced by the superposition of the individual effects, discrepancies between the target c_L and c_M distributions and the AGLA results can also be assigned to deficits

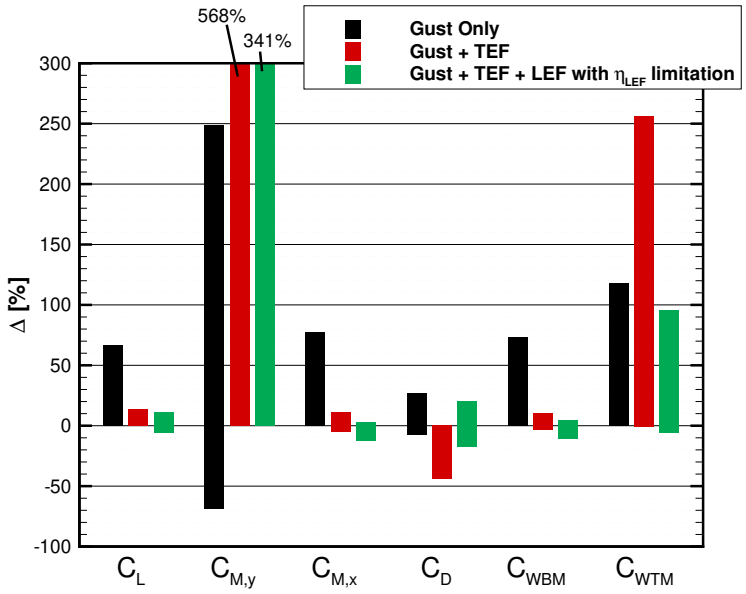

Fig. 17 Maximum changes in the force and moment coefficients as introduced by the reference gust, the TEF deflections at gust inflow conditions, and the combined TEF & LEF at gust inflow condition

in the 2D simulations and the 2D-3D transformation. However, the stated deviations are in an acceptable range when reflecting the assumptions made in the AGLA process and the highly unsteady flow conditions which include unsteady gust interaction, shock induced flow separation, shock buffet etc.

D. Overall Assessment of Gust Loads

In this section the peak loads in all force and moment coefficients, as depicted in Fig. 13, are evaluated in an overall assessment to exclude unintended reactions of the aircraft to TEF and LEF deflections. The evaluation in this section is based on the results of the zonal prediction method presented in the previous section. The bar graph in Fig. 17 illustrates the overall effects on the maxima and minima of the aerodynamic coefficients for the gust-only simulations, the simulations with TEF deflections at gust inflow conditions and the simulations with combined TEF and LEF deflections at gust inflow conditions. Only the results for the case with limited LEF deflections are included for the evaluation of the peak loads. The maximum and minimum loads are evaluated relative to the baseline cruise condition. The lift coefficients clearly correlate with the C_{WBM} even though differences can be noticed in cases where a bad match between the spanwise c_L distribution of the cruise condition and the AGLA case are observed due to the effect of the lever arm on C_{WBM}. As emphasized throughout this work, the positive impact of the TEF deflections on the spanwise c_L alignment and the overall c_L reduction strengthens the assumption of the present work where the fields of aeroelasticity and flight mechanics are neglected. The LEF deflections further reduce the peak in C_L but introduce unsteadiness which can be recognized by the decrease in the minimum C_L. The global pitching moment coefficients

$C_{M,y}$ are evaluated about the center of gravity of the aircraft. As already described in Sec. III.A, the reference gust with λ_{Gust} = 50m induces positive and negative $C_{M,y}$ which are synonymous to nose up and nose down moments, respectively. The center of gravity and the center of pressure are in close proximity to each other, which leads to overall small $C_{M,y}$ values for the baseline cruise case. This explains the rather large percentage difference in $C_{M,y}$ caused by the reference gust and the flap deflections. The TEF deflections eradicate the nose down moment, but introduce a strong increase in the nose up moment. The LEF deflections diminish the overall nose up moment, but the final peak value is still far above the one induced by the gust. However, first estimations have shown that the gust and flap induced changes in $C_{M,y}$ are uncritical as they can be significantly reduced by moderate deflections of the HTP's elevator. As already mentioned, the roll moment of the aircraft $C_{M,x}$ directly correlates to C_{WBM} as the latter represents the roll moment of the wing only about the reference point at the wing root. Thus, a separate assessment is dispensable. The gust generates a horizontal acceleration opposite to the direction of flight, which is characterized by a positive ΔC_D. By adding TEF deflections during the gust encounter a drastic acceleration in flight direction is apparent. The acceleration in flight direction is reduced by the employment of the LEF. Furthermore, a reduction of the positive ΔC_D is introduced. The maximum gust induced ΔC_{WBM} can be reduced by 86% through TEF deflections and an additional reduction by approx. 8% is achieved by including LEF deflections. The LEF deflections introduce a small undershoot in C_{WBM} due to an amplification of gust induced flow separation. A maximum increase in ΔC_{WTM} of about 117% is induced by the TEF deflections which is counterbalanced by the LEF deflection toward 81% of the maximum gust loads. Again, a small undershoot can be observed for the simulations with LEF deflections.

All in all, the overall assessment of the force and moment coefficients suggests a high control authority over the gust induced C_{WBM} as well as the C_{WTM} induced by the gust and TEF deflections. This is feasible in the absence of critical amplifications of the gust induced aerodynamic forces and moments. The increases in the peak loads as introduced by the flaps are smaller or lay in the range as impinged by the gust alone. The large percentage increase in the pitching moment is based on its small reference cruise value and can be mitigated by dynamic deflections of the HTP's elevator.

E. Investigation of Different Extensions and Simplifications of the AGLA Simulation Process

In this section a selection of possible extensions to the described AGLA method, see Sec. II.C, are introduced which are based on efforts to improve the flap scheduling, the capturing of the 3D effects and also simplify the workflow toward the final AGLA simulations. For reasons of clarity the deviations in the peak loads of C_{WBM} and C_{WTM} relative to the baseline cruise condition are compared instead of a comparison of the overall time histories. Furthermore, additional evaluation criteria are considered to assess the unsteadiness introduced by the different AGLA extensions. This is done by an evaluation of the undershoot behavior of C_{WBM} and C_{WTM} through the ratios $C_{WBM,min}/C_{WBM,cruise}$ and $C_{WTM,min}/C_{WTM,cruise}$, respectively. Table 2 contains the results of all methodical extensions discussed below. The

results of the gust simulations without deployed flaps and the results of the standard zonal AGLA method as discussed in Sec. III.C are listed as reference.

The first extension (M 1) comprises a consideration of the zonal time histories of C_{WBM} and C_{WTM} for the flap schedulings. The TEF time functions follow the C_{WBM} time histories of the gust only simulations, see Fig. 6. The LEF time functions are based on the C_{WTM} time histories resulting from the TEF simulations at gust conditions as depicted in Fig. 14. This adaption of the initial "1 − cos" flap scheduling allows to mirror the actual load response of the wing sections to the gust and the TEF deflections. The mentioned time responses differ partly significantly from a "1 − cos" shape due to the larger decay times, phase shifts and flow separation. The flap deflection angles are kept identical to the reference case (zonal method) to allow to determine the pure influence of the flap time functions on the load alleviation. The results reveal a deterioration of the C_{WBM} compensation characteristics in both maximum loads and undershoot behavior, see M 1 in Table 2. This is ascribable to the rather unsmooth flap time functions with alternatingly decreasing and increasing deflection angles. The TEF induced C_{WTM} is somewhat overcompensated by the adapted time function. However, when compared to the zonal method, an improved agreement with the target ΔC_{WTM} of 118.30% (gust effect only) is achieved. To clarify, it is not excluded that a time function which considers the load response characteristics of the wing zones can be used for a better attenuation of gust loads. However, a smoothing of the flap time functions might be necessary to exclude undesired unsteady effects.

The second method (M 2) simplifies the zonal method by only evaluating the global time histories on the overall wing. This allows to reduce the evaluation effort significantly. The spanwise loads along the full wing span are evaluated at the time of the maximum gust induced C_{WBM} and gust + TEF induced C_{WTM}. The neglect of the zonal wing loads leads to an improved compensation of ΔC_{WBM} by similar undershoot behavior as the standard zonal approach. The prediction of the required LEF angles for the ΔC_{WTM} alleviation as introduced by the TEF is also improved when compared to the zonal approach. At the same time, no major increase in the unsteadiness of C_{WTM} is deducible. The reasons for the improvement with the global evaluation approach are rather inexplicable and thus a random interaction of different unsteady effects is assumed to be the reason for this. Nevertheless, it can be said that a similar efficiency of the AGLA is possible by the global approach when compared to the zonal approach. The approximation of flap amplitudes from evaluation of gust loads at the full wing leads to similar results as the evaluation of gust loads at five spanwise wing zones. This necessitates a nearly simultaneous occurrence of the maximum loads along full wing span.

Table 2 Summary of different gust alleviation strategies regarding their impact on C_{WBM} and C_{WTM}.

	Gust	Zonal Method	M 1	M 2	M 3	M 4	M 5	M 6
ΔC_{WBM} [%]	77.76	3.15	5.93	0.01	6.91	0.00	16.53	10.11
$C_{WBM,min}/C_{WBM,cruise}$ [%]	-0.57	-12.49	-32.32	-14.33	-8.88	-22.42	-33.12	-33.52
ΔC_{WTM} [%]	118.30	96.07	111.49	113.50	113.76	104.33	114.51	118.29
$C_{WTM,min}/C_{WTM,cruise}$ [%]	-1.05	-5.65	-3.13	-6.96	-3.94	-14.18	-15.61	-1.61

However, the applicability of the global load evaluation may depend on the gust load scenario, inflow conditions and the aircraft configuration which means that these results can not be generalized.

The third method (M 3) is also a simplification of the standard zonal approach. Here, the 3D TEF and LEF amplitudes are directly derived from the 2D database without the utilization of presimulations with deflected TEF only. This saves the second step of 3D simulations illustrated in Fig. 4 and thus 1/3 of the computation time for the overall routine. This simplification is strongly dependent on a good ability to superimose the TEF and LEF effects as well as a good transferability between 2D and 3D results. The small phase lags in C_{WTM} introduced by the TEF deflections facilitate the implementation of the direct approach. The results indicate similar overall load reductions when compared to the standard zonal approach with somewhat improved undershoot behavior and improved ΔC_{WTM} prediction. The peak in C_{WBM} exceeds the level of the zonal approach by approx. 3.8%. Overall, the results reveal a sound prediction without the necessity of presimulations with deflected TEF. Again, an identification of reasons for the small deviations between the zonal approach and M 2 is not straightforward due to the complexity of the problem. Therefore, we state that the direct approach allows similar AGLA capacities as the zonal approach and the global approach (M 2) without providing a detailed explanation.

The fourth method (M 4) is based on an extension to compensate inaccuracies which are incorporated during the application of the 2.5D swept-wing theory for the estimation of the 3D TEF efficiencies. This comprises the neglect of finite wing span, assumptions made for the used effective wing sweep, wing tapering and 3D root effects. As already mentioned in Sec. III.B, no correction of the 2D data is considered to cover the effects of the trailing vortices which are strong in case of discrete TEF deflections or significant variations in the spanwise TEF deflections. This means a similarity in $\alpha_{2.5D}$ and α_{3D} is presumed by neglecting the induced angle of attacks of the trailing vortices. The subscript 2.5D denotes 2D simulation data which is transformed into the line of flight wing section through standard swept-wing theory transformation and the line of the 50% c as effective sweep angle, see Eq. (4. We make the assumption that the inaccuracies in the 2D-3D transformations regarding efficiencies of continuous TEF can be derived from differences in the local lift gradients. The gradients from the 2D airfoil simulations $dc_{L2.5D}/d\alpha_{2.5D}$ and the 3D aircraft simulations $dc_{L,3D}/d\alpha_{3D}$ are extracted from 2D and 3D angle of attack polar computations. The assumption is reasonable in case the quotient of $dc_L/d\alpha$ and $dc_L/d\eta$ are similar between 2D and 3D TEF deflections. This is the case for the investigated α and η ranges. The correction is applied to the TEF deflection angles by the following equation:

$$\frac{dc_{L,3D}}{d\eta_{TEF,3D}} = \frac{dc_{L,3D}}{d\alpha_{3D}} \frac{dc_{L,2.5D}}{d\eta_{TEF,2.5D}} \frac{1}{\frac{dc_{L,2.5D}}{d\alpha_{2.5D}}} \rightarrow \Delta\eta_{TEF,3D} = \Delta c_{L,3D} \frac{dc_{L,2.5D}}{d\alpha_{2.5D}} \frac{dc_{L,2.5D}}{d\eta_{TEF,2.5D}} \frac{1}{\frac{dc_{L,3D}}{d\alpha_{3D}}} \tag{7}$$

$$with \quad \eta_{TEF,2.5D} = \eta_{TEF,3D} \quad \& \quad \alpha_{2.5D} = \alpha_{3D}$$

The values for the flap efficiency gradients $dc_{L2.5D}/d\eta_{TEF,2.5D}$ and $dc_{M2.5D}/d\eta_{LEF,2.5D}$ can be derived from the 2D database at the respective airfoil sections, see Fig. 11, and a subsequent 2.5D transformation. These gradients are mostly

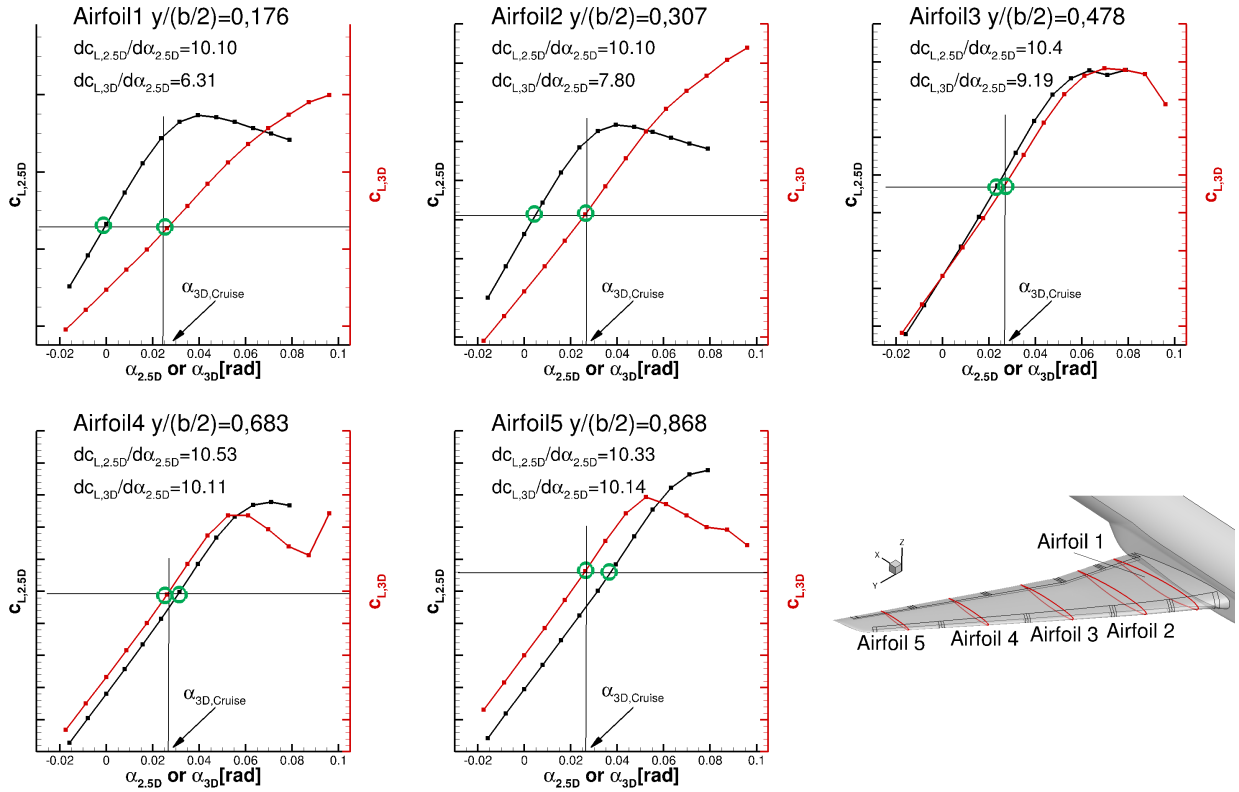

Fig. 18 2.5D and 3D local c_L polars with extracted gradients for extension method 4.

uniform in the range of selected flap angles except for large LEF deflections. The local 2D and 3D α-polars of c_L as derived from the 2D and 3D results are depicted in Figs. 18. A large discrepancy in the gradients can be observed at the two inboard airfoil sections. On the one hand this is attributable to strong 3D wing root effects due to the presence of the fuselage and the related endplate effects. On the other hand the lack of the selected effective wing sweep to represent the wing sweep of the inboard wing ($y < y_{kink}$) contributes also to the bad match in the local c_L gradients. Even though the endplate effects are somewhat captured by considering the local 3D lift value at standard cruise for the 2D computations by an α-iteration, the root effects are subject to changes based on the effective angle of attack induced by the gust effect and flap deflections. The gradients of the 3D c_L polars inboard of the wing kink are smaller than the gradients of the 2D c_L polars. Therefore, the correction factor for the 3D TEF efficiencies is positive at the inboard wing. This is conform to the results presented in Fig. 10, where the 2D TEF deflections show a clearly higher efficiency compared to the results of the continuous 3D TEF deflections. A quite good agreement in the 2D and 3D c_L gradient is visible outboard from the wing kink, which encourages our selection of the 50%c line for the effective wing sweep angle. Furthermore, the results predict a small impact due to the neglect of the wing tip effects (finite wing span) and the wing tapering. The gradients $dc_{L,2.5D}/d\alpha_{2.5D}$ and $dc_{L,3D}/d\alpha_{3D}$ are extracted at the c_L obtained at the α for 3D cruise conditions, see green circled data points in Fig. 18. The application of the 3D corrections lead to the TEF

angles listed in line 1 of Table 3. The most inboard TEF deflection is corrected by $\Delta\eta_{TEF} = -4.74°$ when compared to the reference approach (see Table 1) while the 3D correction is significantly reduced at the outboard wing. The increased inboard TEF deflections lead to an increase in the required LEF deflection angle, see second data line in Table 3. The higher LEF deflections at the inboard wing lead to an increased vulnerability toward flow separation and thus to a deterioration of the AGLA approach. The 3D corrections lead to a further reduction of ΔC_{WBM} towards a full mitigation of the gust loads. However, the correction does not improve the undershoot behavior, which is intensified by an overall shift of the C_{WBM} time curve towards smaller values. A small improvement is also discernible with regard to the ΔC_{WTM} prediction but again at the expense of the unsteady undershoot behavior. The overshoot in C_{WTM} is induced by the higher inboard LEF deflections. From the theoretic perspective the presented 3D correction based on the dc_L-α gradients is reasonable, but due to the large correction required for η_{LEF}, the approach is not feasible.

Table 3 TEF deflection angles η resulting from correction method 4.

Case	η_{TEF1}	η_{TEF2}	η_{TEF3}	η_{TEF4}	η_{TEF5}	η_{LEF1}	η_{LEF2}	η_{LEF3}	η_{LEF4}	η_{LEF5}
TEF Only	-12.5°	-11.9°	-10.3°	-9.6°	-8.2°	0°	0°	0°	0°	0°
TEF + LEF	-11.0°	-10.4°	-9.3°	-8.9°	-7.9°	20.5°	22.8°	15.5°	11.4°	5.8°

The final two listed methods (M 5 and M 6) are added to illustrate the impact of an inadequate consideration of the aerodynamic phase shifts. Phase shifts in the order as introduced by the delayed gust response and the delayed reaction to TEF deflections are introduced as phase lags (M 5) and phase leads (M 6). A clear deterioration in the ΔC_{WBM} capacity and in the unsteady behavior of C_{WBM} can be seen when compared to the reference zonal approach where a correct consideration of the existing phase shifts is applied for the flap schedulings. The improved agreement in ΔC_{WTM} with the gust results is again rather a coincidence than a result of an improved control through a different phase shift. The same applies to the smaller undershoot in C_{WTM} for M 6. The results clearly demonstrate the importance of a correct consideration of the geometric and aerodynamic phase shifts which result from the wing sweep and the delayed aerodynamic responses to the gust and the flap deflections. The out of phase flap scheduling is clearly prone to an amplification of the unsteady aerodynamic effects.

All in all, the presented extensions and simplifications give an overview of their impacts on the AGLA efficiency. The modifications of the standard zonal approach demonstrate that the steps required by the initial zonal AGLA approach can be reduced if the following applies: (1) The peak loads occur simultaneously along the wing span (2) the ability to superimpose the gust, TEF and LEF effects is solid and (3) the 2D-3D transformation is applicable. The optimization of the flap scheduling by employing the zonal loads along the wing span does not lead to an improved load alleviation due to the resulting non-smooth time histories. The 3D corrections show a clear capacity of improvement for the

standard zonal approach. However, the large 3D corrections lead to unfeasible inboard LEF deflections. Finally, a correct monitoring and subsequent application of the phase shifts is essential for a solid AGLA concept.

IV. Conclusions

The present work summarizes efforts to mitigate loads induced by an idealized "1− cos"-type gust event during transonic cruise conditions. Spanwise segmented dynamic TEF and LEF on a generic aircraft configuration are used to mitigate structural wing loads which are represented by the WBM and the WTM. A mono-disciplinary approach based on CFD-standalone simulations is used to compute the aerodynamic effects accompanied by gust-aircraft interaction with and without flap deflections. A concept based on parametric 2D simulations is introduced to provide a practicable prediction method for required TEF and LEF deflections for mitigation of gust induced wing loads. The 2D studies enable an estimation of the required 3D flap deflections for a full compensation of the gust loads.

A gust wavelength study based on FAA FAR-25 norm reveals that a vertical "1− cos" gust with a wavelength of 50 m can be chosen as the critical gust scenario. A detailed analysis of the gust induced wing loads on spanwise confined wing zones reveals significant differences along the wing span based on the impact of local flow separation, local chord extension and the spanwise lever arm. The AGLA approach is validated through a selected set of simulations, which proves the general ability to superimpose the aerodynamic effects caused by the gust, the TEF and the LEF as well as the 2D-3D data transferability. Only, the prevailing flow separation at gust interaction causes some deficiencies in the ability to superimpose the gust and the flap effects. The 2D database is generated at five spanwise representative wing sections by considering an extended wing sweep theory which covers dependencies on the local Reynolds number and local chordwise extensions of the flaps. It is shown that the flap characteristics derived from the 2D simulations, which comprise a high efficiency of the TEF and LEF for control of the WBM and WTM, respectively, are mostly applicable to the 3D configuration, both qualitatively and quantitatively. Moderate TEF deflections allow a nearly full compensation of the transient gust loads with regard to the WBM. The upward directed TEF deflections amplify the gust induced local nose up moment which can't be fully mitigated through appropriate LEF deflections. LEF deflections in the required range for a full control of the gust and TEF induced WTM trigger large scale flow separation. A limitation of the LEF deflections allows to compensate WTM on the order as induced by the TEF deflections alone. Unsteady phenomena that are attributable to the complex aircraft-gust-flap interactions are prevailing at transonic speeds which introduce undershoot and overshoot characteristics in the temporal aircraft reaction.

Extensions of the standard prediction method for the 3D flap deflections are introduced to assess the impact of the assumptions made for the extended wing sweep theory. Furthermore, a major impact of the flap schedulings and the phase shifts is revealed. A substantial deterioration of the AGLA capacity is apparent in case one of the aerodynamic phase lags is neglected. The aerodynamic phase lags comprise the delayed response to the gust and the flaps. These phase lags are similar in size but opposed to each other. Thus, a simple consideration of the geometric phase lag

introduced by the wing sweep is sufficient to obtain a representative response to the AGLA by dynamic flaps. Flap time functions which mirror the response of the spanwise wing sections to the gust instead of the "1-cos" gust shape lead to disadvantages in the unsteady gust response. A great saving in computation and post-processing time is possible in case of a solid ability to superimpose the gust, TEF and LEF effects as well as a nearly simultaneous occurrence of peak loads along the wing span.

Overall, the simulation results reveal a high control authority of gust induced WBM and WTM through dynamic TEF and LEF deflections. Simultaneously, the impact on the other forces and moments acting on the aircraft can be kept smaller or in the range as induced by the gust alone. The standard AGLA approach allows a reduction in the gust induced WBM by 86% through TEF deflections and an additional reduction by approx. 8% by the addition of LEF deflections. The gust induced WTM is only reduced by 19% due to the aforementioned effect of the upward directed TEF on the WTM. The assessment of additional improvements of the WBM and WTM mitigation through the presented extended approaches are limited due to the large influence of nonlinear aerodynamic effects such as shock induced flow separation. However, improvements through an optimal exploitation of the spanwise loads and their contributions to the wing loads are feasible. A further insight into the complex flow physics related to the unsteady phenomena accompanied by gust-aircraft-flap interactions will allow a further optimization of the presented AGLA method. Additionally, an application of the presented concept at lower maximum vertical gust velocities and subsonic flow conditions will reveal the limitations of the AGLA approach at a more linear flow regime.

V. Acknowledgments

The research which led to the presented results is funded by the Federal Ministry for Economic Affairs and Climate Action as part of the LuFo project PoLamin ("**Po**tenziale für drastische **La**st**min**derung bei Verkehrsflugzeugen"). The authors gratefully acknowledge the support and the computational resources which were provided by the High Performance Computing Center Stuttgart (HLRS). Special thanks are also due to the DLR (Institute of Aerodynamics and Flow Technology) for providing the research configuration.

References

[1] Graver, B., Rutherford, D., and Zheng, S., "CO_2 Emissions From Commercial Aviation: 2013, 2018, and 2019," 2020. International Council on Clean Transportation.

[2] Xu, J., and Kroo, I., "Aircraft design with active load alleviation and natural laminar flow," *Journal of Aircraft*, Vol. 51, No. 5, 2014, pp. 1532–1545. American Institute of Aeronautics and Astronautics.

[3] U.S. Department of Transportation, "Federal Aviation Regulations, Part 25: airworthiness standards: transport category air-planes," Federal Aviation Administration, 1996, Section 341: Gust and Turbulence Loads.

[4] Vega, H., "Investigation of load alleviation in aircraft pre-design and its influence on structural mass and fatigue," *Aerospace Science and Technology*, Vol. 122, 2022, p. 107405. doi:https://doi.org/10.1016/j.ast.2022.107405.

[5] Regan, C. D., and Jutte, C. V., *Survey of Applications of Active Control Technology for Gust Alleviation and New Challenges for Lighter-weight Aircraft*, Dryden Flight Research Center, Edwards, California, NASA/TM-2012-216008, 2012.

[6] Hübner, A.-R., and Reimer, L., *Multidisciplinary Simulation for Gust Load Alleviation Control Surface Analysis*, New Results in Numerical and Experimental Fluid Mechanics XII, Publisher: Springer, 2019, pp. 576–585. doi:10.1007/978-3-030-25253-3_55.

[7] Klug, L., Radespiel, R., Ullah, J., Seel, F., Lutz, T., Wild, J., Heinrich, R., and Streit, T., "Actuator concepts for active gust alleviation on transport aircraft at transonic speeds," *AIAA Scitech 2020 Forum, 6-10 January 2020 Orlando, Florida*, 2020. doi:10.2514/6.2020-0271, AIAA paper 2020-0271.

[8] Thornton, S. V., "Reduction of structural loads using maneuver load control on the advanced fighter technology integration (AFTI)/F-111 mission adaptive wing," 1993. NASA TM 4526.

[9] Pena, F., Martins, B. L., and Richards, W. L., "Active in-flight load redistribution utilizing fiber-optic shape sensing and multiple control surfaces," 2018. NASA/TM-2018-219741.

[10] Rennie, R., and Jumper, E., "Experimental measurements of dynamic control surface effectiveness," *Journal of Aircraft*, Vol. 33, No. 5, 1996, pp. 880–887.

[11] Rennie, R., and Jumper, E., "Gust alleviation using trailing-edge flaps," *37th Aerospace Sciences Meeting and Exhibit*, 1999. doi:10.2514/6.1999-649, AIAA paper 99-0649.

[12] Zhu, W. J., Shen, W. Z., and Sørensen, J. N., "Numerical investigation of flow control feasibility with a trailing edge flap," *Journal of Physics: Conference Series*, Vol. 524, IOP Publishing, 2014, p. 012102.

[13] Shao, K., Wu, Z., Yang, C., Chen, L., and Lv, B., "Design of an adaptive gust response alleviation control system: simulations and experiments," *Journal of Aircraft*, Vol. 47, No. 3, 2010, pp. 1022–1029.

[14] Rennie, R., and Jumper, E., "Dynamic leading-edge flap scheduling," *Journal of aircraft*, Vol. 34, No. 5, 1997, pp. 606–611.

[15] Miller, E. J., Lokos, W. A., Cruz, J., Crampton, G., Stephens, C. A., Kota, S., Ervin, G., and Flick, P., "Approach for structurally clearing an adaptive compliant trailing edge flap for flight," *Society of Flight Test Engineers International Annual Symposium, Lancaster, CA; United States*, 2015.

[16] Prachař, A., Hospodář, P., and Vrchota, P., "Gust Alleviation of Aeroelastic Aircraft Using CFD Simulation," *Transportation Research Procedia*, Vol. 29, 2018, pp. 366–375. Publisher: Elsevier.

[17] Ullah, J., Seel, F., and Lutz, T., "Numerical Study of Dynamic 2D Bumps for Active Gust Load Alleviation," *STAB/DGLR Symposium*, Springer, 2020, pp. 257–268.

[18] Khalil, K., Asaro, S., and Bauknecht, A., "Active flow control devices for wing load alleviation," *Journal of Aircraft*, Vol. 59, No. 2, 2022, pp. 458–473.

[19] Wang, X., Mkhoyan, T., Mkhoyan, I., and De Breuker, R., "Seamless active morphing wing simultaneous gust and maneuver load alleviation," *Journal of Guidance, Control, and Dynamics*, Vol. 44, No. 9, 2021, pp. 1649–1662.

[20] Castrichini, A., Cooper, J. E., Wilson, T., Carrella, A., and Lemmens, Y., "Nonlinear negative stiffness wingtip spring device for gust loads alleviation," *Journal of Aircraft*, Vol. 54, No. 2, 2017, pp. 627–641.

[21] Cheung, R. C., Rezgui, D., Cooper, J. E., and Wilson, T., "Testing of a hinged wingtip device for gust loads alleviation," *Journal of Aircraft*, Vol. 55, No. 5, 2018, pp. 2050–2067.

[22] Cheung, R. C., Rezgui, D., Cooper, J. E., and Wilson, T., "Testing of Folding Wingtip for Gust Load Alleviation of Flexible High-Aspect-Ratio Wing," *Journal of Aircraft*, Vol. 57, No. 5, 2020, pp. 876–888.

[23] Sanghi, D., Riso, C., Cesnik, C. E., and Vetrano, F., "Conventional and Unconventional Control Effectors for Load Alleviation in High-Aspect-Ratio-Wing Aircraft," *AIAA SCITECH 2022 Forum*, 2022, p. 4093.

[24] Hashemi, K. E., Nguyen, N. T., Drew, M. C., Chaparro, D., and Ting, E., "Performance optimizing gust load alleviation control of flexible wing aircraft," *2018 AIAA Guidance, Navigation, and Control Conference*, 2018, p. 0623.

[25] Wang, X., Van Kampen, E., Chu, Q., and De Breuker, R., "Flexible aircraft gust load alleviation with incremental nonlinear dynamic inversion," *Journal of Guidance, Control, and Dynamics*, Vol. 42, No. 7, 2019, pp. 1519–1536.

[26] Stanford, B. K., "Optimization of an aeroservoelastic wing with distributed multiple control surfaces," *Journal of Aircraft*, Vol. 53, No. 4, 2016, pp. 1131–1144.

[27] Yagil, L., Raveh, D. E., and Idan, M., "Deformation control of highly flexible aircraft in trimmed flight and gust encounter," *Journal of Aircraft*, Vol. 55, No. 2, 2018, pp. 829–840.

[28] Ferrier, Y., Nguyen, N. T., Ting, E., Chaparro, D., Wang, X., de Visser, C. C., and Chu, Q. P., "Active gust load alleviation of high-aspect ratio flexible wing aircraft," *2018 AIAA Guidance, Navigation, and Control Conference*, 2018, p. 0620.

[29] Livne, E., "Aircraft active flutter suppression: State of the art and technology maturation needs," *Journal of Aircraft*, Vol. 55, No. 1, 2018, pp. 410–452.

[30] Fezans, N., Joos, H.-D., and Deiler, C., "Gust load alleviation for a long-range aircraft with and without anticipation," *CEAS Aeronautical Journal*, Vol. 10, No. 4, 2019, pp. 1033–1057.

[31] Fournier, H., Massioni, P., Tu Pham, M., Bako, L., Vernay, R., and Colombo, M., "Robust Gust Load Alleviation of Flexible Aircraft Equipped with Lidar," *Journal of Guidance, Control, and Dynamics*, Vol. 45, No. 1, 2022, pp. 58–72.

[32] Ullah, J., Kamoun, S., Müller, J., and Lutz, T., "Active Gust Load Alleviation by Means of Steady and Dynamic Trailing and Leading Edge Flap Deflections at Transonic Speeds," *AIAA ScTech 2022 Forum, 3–7 January 2022, San Diego, CA*, 2022. doi:10.2514/6.2022-1334, AIAA paper 2022-1334.

[33] Ullah, J., Lutz, T., Klug, L., Radespiel, R., and Wild, J., "Active Gust Load Alleviation by Combined Actuation of Trailing Edge and Leading Edge Flap at Transonic Speeds," *AIAA Scitech 2021 Forum, 11–15 19–21 January 2021, Virtual Event*, 2021. doi:10.2514/6.2021-1831, AIAA paper 2021-1831.

[34] Wild, J., Pott-Pollenske, M., and Nagel, B., "An integrated design approach for low noise exposing high-lift devices," *3rd AIAA Flow Control Conference*, 2006. doi:10.2514/6.2006-2843, AIAA paper 2006-2843.

[35] Dargel, G., Hansen, H., Wild, J., Streit, T., Rosemann, H., and Richter, K., "Aerodynamische Flügelauslegung mit multifunktionalen Steuerflächen," *DGLR Jahrbuch 2002, DGLR-2002-096, Band I, DGLR, pp. 1605ff*, 2002.

[36] Schwamborn, D., Gerhold, T., and Heinrich, R., "The DLR TAU-code: Recent applications in research and industry," *ECCOMAS CFD 2006 CONFERENCE*, eds. P. Wesseling , E. Oñate , J. Périaux, TU Delft Publisher, ISBN 90-9020970-0, 2006.

[37] Michler, A. K., "Aircraft control surface deflection using RBF-based mesh deformation," *International Journal for Numerical Methods in Engineering*, Vol. 88, No. 10, 2011, pp. 986–1007.

[38] McDaniel, D., Sears, D., Tuckey, T., Tillman, B., and Morton, S., "Aerodynamic control surface implementation in kestrel v2. 0," *49th AIAA Aerospace Sciences Meeting including the New Horizons Forum and Aerospace Exposition*, 2011. doi:10.2514/6.2011-1175, AIAA paper 2011-1175.

[39] Heinrich, R., and Reimer, L., "Comparison of different approaches for gust modeling in the CFD Code TAU," *International Forum on Aeroelasticity and Structural Dynamics, Bristol, UK*, Royal Aeronautical Society ISBN: 978-1-63439-102-3, Vol. 3, 2013.

[40] Müller, J., Hillebrand, M., and Lutz, T., "Assessment of the Disturbance Velocity Approach to Determine the Gust Impact on Airfoils in Transonic Flow," *New Results in Numerical and Experimental Fluid Mechanics XIII*, edited by A. Dillmann, G. Heller, E. Krämer, and C. Wagner, Springer International Publishing, Cham, 2021, pp. 14–23.

[41] Müller, J., Hillebrand, M., Schollenberger, M., Ehrle, M., Lutz, T., and Krämer, E., "Studies on the Applicability of a Simplified Gust Simulation Approach in the CFD Code TAU," *High Performance Computing in Science and Engineering '20*, edited by W. E. Nagel, D. H. Kröner, and M. M. Resch, Springer, Cham, 2021. Submitted for publication.

[42] Reimer, L., Ritter, M., Heinrich, R., and Krüger, W., "CFD-based Gust Load Analysis for a Free-flying Flexible Passenger Aircraft in Comparison to a DLM-based Approach," *22nd Computational Fluid Dynamics Conference, Dallas, TX, USA*, 2015. doi:10.2514/6.2015-2455, AIAA paper 2015-2455.

[43] Reimer, L., Heinrich, R., and Ritter, M., "Towards Higher-Precision Maneuver and Gust Loads Computations of Aircraft: Status of Related Features in the CFD-Based Multidisciplinary Simulation Environment FlowSimulator," *New Results in Numerical and Experimental Fluid Mechanics XII, Publisher: Springer*, 2020, pp. 597–607. doi:10.1007/978-3-030-25253-3_57.

[44] Schlichting, H., and Truckenbrodt, E., *Aerodynamik des Flugzeuges: Zweiter Band: Aerodynamik des Tragflügels (Teil II), des Rumpfes, der Flügel-Rumpf-Anordnung und der Leitwerke*, Springer-Verlag, 2001.

[45] Bendiksen, O. O., "Review of unsteady transonic aerodynamics: Theory and applications," *Progress in Aerospace Sciences*, Vol. 47, No. 2, 2011, pp. 135–167. doi:https://doi.org/10.1016/j.paerosci.2010.07.001.

[46] Pätzold, H. M., *Auslegungsstudien zu 3-D shock-control-bumps mittels numerischer optimierung*, 2009. Publisher: Verlag Dr. Hut.

[47] Streit, T., Wichmann, G., von Knoblauch zu Hatzbach, F., and Campbell, R., "Implications of conical flow for laminar wing design and analysis," *29th AIAA Applied Aerodynamics Conference*, 2011. doi:10.2514/6.2011-3808, AIAA paper 2011-3808.

[48] Lock, R., "The aerodynamic design of swept winged aircraft at transonic and supersonic speeds," *The Aeronautical Journal*, Vol. 67, No. 630, 1963, pp. 325–337.

[49] Zhao, T., Zhang, Y., Chen, H., Chen, Y., and Zhang, M., "Supercritical wing design based on airfoil optimization and 2.75D transformation," *Aerospace Science and Technology*, Vol. 56, 2016, pp. 168–182. doi:https://doi.org/10.1016/j.ast.2016.07.010.

[50] Knoblach, A., and Looye, G., "Efficient Determination of Worst-Case Gust Loads Using System Norms," *Journal of Aircraft*, Vol. 54, No. 3, 2017, pp. 1205–1210.

[51] Fournier, E., Grihon, S., Bes, C., and Klein, T., "Prediction of Preliminary Maximum Wing Bending Moments Under Discrete Gust," *Journal of Aircraft*, Vol. 56, No. 4, 2019, pp. 1722–1725.

[52] Mallik, W., and Raveh, D. E., "Gust Response at High Angles of Attack," *AIAA Journal*, Vol. 57, No. 8, 2019, pp. 3250–3260.

[53] Fezans, N., and Joos, H.-D., "Combined feedback and Lidar-based Feedforward Active Load Alleviation," *AIAA Atmospheric Flight Mechanics Conference*, 2017. doi:10.2514/6.2017-3548, AIAA paper 2017-3548.

[54] Neumann, J., "Zum Nachweis der Superponierbarkeit instationärer Luftkräfte beim Böenantwortproblem," Tech. Rep. DLR IB 232-2012, February 2012. URL `https://elib.dlr.de/75047/`.

[55] Leishman, J. G., "Unsteady lift of a flapped airfoil by indicial concepts," *Journal of Aircraft*, Vol. 31, No. 2, 1994, pp. 288–297.